

DUDLEY KNOX LIBRARY
NAVAL POSTGRADUATE SCHOOL
MONTEREY, CALIFORNIA 93943-5003

NAVAL POSTGRADUATE SCHOOL

Monterey, California



THESIS

INVESTIGATION OF A MACH 1.4 COMPRESSOR
CASCADE WITH VARIABLE BACK PRESSURE
USING FLOW VISUALIZATION

by

Michael George Hegland

March 1986

Thesis Advisor:

Raymond P. Shreeve

Approved for public release; distribution is unlimited.

T226325

REPORT DOCUMENTATION PAGE

1. REPORT SECURITY CLASSIFICATION Unclassified			1b. RESTRICTIVE MARKINGS			
2. SECURITY CLASSIFICATION AUTHORITY			3. DISTRIBUTION / AVAILABILITY OF REPORT Approved for public release; distribution is unlimited			
4. CLASSIFICATION / DOWNGRADING SCHEDULE			5. MONITORING ORGANIZATION REPORT NUMBER(S)			
6. PERFORMING ORGANIZATION REPORT NUMBER(S)			7a. NAME OF MONITORING ORGANIZATION Naval Postgraduate School			
7. NAME OF PERFORMING ORGANIZATION Naval Postgraduate School		8b. OFFICE SYMBOL (If applicable) Code 67		7b. ADDRESS (City, State, and ZIP Code) Monterey, California 93943-5000		
8. ADDRESS (City, State, and ZIP Code) Monterey, California 93943-5000		9. PROCUREMENT INSTRUMENT IDENTIFICATION NUMBER		10. SOURCE OF FUNDING NUMBERS		
9. NAME OF FUNDING / SPONSORING ORGANIZATION		8b. OFFICE SYMBOL (If applicable)		10. SOURCE OF FUNDING NUMBERS		
10. ADDRESS (City, State, and ZIP Code)		PROGRAM ELEMENT NO.		PROJECT NO.		WORK UNIT ACCESSION NO.
11. TITLE (Include Security Classification) Investigation of a Mach 1.4 Compressor Cascade with Variable Back Pressure Flow Visualization						
12. PERSONAL AUTHOR(S) Land, Michael G.						
13. TYPE OF REPORT Master's Thesis		13b. TIME COVERED FROM _____ TO _____		14. DATE OF REPORT (Year, Month, Day) 1986, March		15. PAGE COUNT 115
16. SUPPLEMENTARY NOTATION						
17. COSATI CODES			18. SUBJECT TERMS (Continue on reverse if necessary and identify by block number)			
FIELD	GROUP	SUB-GROUP	Transonic Compressor Cascade Flow Visualization			
19. ABSTRACT (Continue on reverse if necessary and identify by block number)						
Flow through a transonic compressor cascade model was investigated at Mach 1.4 using flow visualization and pressure measurements. Shock patterns at two different blade incidences were documented at increasing back pressures. Data were taken up to a maximum pressure ratio of 1.53 at estimated minimum loss incidence conditions. An oblique shock system existed, producing large flow turning (6.8°) and a slightly supersonic flow at Mach number (1.02). Losses and blade pressure loading were calculated using a combination of test data and computational approximations. Failure of blade retaining tabs occurred with both aluminum and steel cascade models. Failures were attributed to fatigue from high oscillatory stress levels and redesigned blade mounts were proposed.						
20. DISTRIBUTION / AVAILABILITY OF ABSTRACT UNCLASSIFIED/UNLIMITED <input type="checkbox"/> SAME AS RPT. <input type="checkbox"/> DTIC USERS				21. ABSTRACT SECURITY CLASSIFICATION Unclassified		
22a. NAME OF RESPONSIBLE INDIVIDUAL Prof. Raymond P. Shreeve				22b. TELEPHONE (Include Area Code) (408) 646-2593		22c. OFFICE SYMBOL Code 67Sf

Approved for public release; distribution is unlimited.

Investigation of a Mach 1.4
Compressor Cascade with Variable
Back Pressure Using Flow Visualization

by

Michael George Hegland
Lieutenant Commander, United States Navy
B.S., Western Washington University, 1975

Submitted in partial fulfillment of the
requirements for the degree of,

MASTER OF SCIENCE IN AERONAUTICAL ENGINEERING

from the

NAVAL POSTGRADUATE SCHOOL
March 1986

ABSTRACT

Flow through a transonic compressor cascade model was investigated at $M = 1.4$ using flow visualization and pressure measurements. Shock patterns for two different blade incidences were documented at increasing back pressures. Data were taken up to a maximum pressure ratio of 1.53 at estimated minimum loss incidence conditions. An oblique shock system persisted, producing large flow turning (6.8°) and a slightly supersonic exit mach number (1.02). Losses and blade pressure loading were calculated using a combination of test data and computational approximations. Failure of blade retaining tabs occurred with both aluminum and steel cascade blades. Failures were attributed to fatigue from high oscillatory stress levels and redesigned blade mounts were proposed.

1/23
H
1

TABLE OF CONTENTS

I.	INTRODUCTION -----	13
II.	APPARATUS AND INSTRUMENTATION -----	15
	A. GENERAL DESCRIPTION -----	15
	B. BACK PRESSURE CONTROL -----	16
	C. POROUS WALL MASS FLOW CONTROL -----	17
	D. CASCADE BLADES -----	17
	E. OSCILLATION MEASUREMENT EQUIPMENT DESIGN -----	18
III.	EXPERIMENTAL PROGRAM AND PROCEDURES -----	20
	A. PRELIMINARY TESTS -----	20
	B. BACK PRESSURE VARIATION AND WAVE CANCELLATION: PHASE 1 -----	20
	C. BACK PRESSURE VARIATION AND WAVE CANCELLATION: PHASE 2 -----	21
	D. TEST PROCEDURES -----	22
IV.	RESULTS AND DISCUSSION -----	23
	A. GENERAL FLOW CHARACTERISTICS -----	23
	B. WAVE CANCELLATION -----	26
	C. CASCADE DESIGN AND PERFORMANCE -----	26
	D. BLADE FAILURES -----	28
V.	CONCLUSIONS AND RECOMMENDATIONS -----	31
	APPENDIX A: OPTICAL SYSTEM OPTIMIZATION -----	59
	APPENDIX B: BACK PRESSURE CONTROL -----	70
	APPENDIX C: FLOW OSCILLATION MEASUREMENT EQUIPMENT -----	76

APPENDIX D: TRANSONIC COMPRESSOR CASCADE
OPERATING PROCEDURES ----- 83

APPENDIX E: ANALYSIS OF EXPERIMENTAL DATA ----- 85

APPENDIX F: ANALYSIS FROM DESIGN DATA ----- 94

APPENDIX G: TEST DATA ----- 99

LIST OF REFERENCES ----- 111

INITIAL DISTRIBUTION LIST ----- 114

LIST OF TABLES

I.	PLEXIGLAS SIDEWALL STATIC PRESSURE TAP LOCATIONS -----	34
II.	MECHANICAL PROPERTIES OF 7075-T6 ALUMINUM AND 4340 STEEL -----	35
III.	CASCADE BLADING DESIGN PARAMETERS -----	35
C.1.	HUV-1100BQ OPERATING DATA AND PERFORMANCE SPECIFICATIONS -----	78
E.1.	CHANGES ACROSS SHOCKS IMPINGING ON THE UPPER NOZZLE SURFACE -----	89
E.2.	CHANGES ACROSS PASSAGE SHOCKS FROM BLADES 2, 3 AND 4 -----	89
E.3.	SUCTION SURFACE FLOW CHARACTERISTICS -----	90
E.4.	PRESSURE SURFACE FLOW CHARACTERISTICS -----	90
E.5.	BLADE PASSAGE EXIT FLOW CHARACTERISTICS -----	90
E.6.	BLADE PASSAGE MASS FLOW -----	91
F.1.	CALCULATED LOSS COEFFICIENTS -----	98
G.1.	CASCADE TEST 5246-1 -----	100
G.2.	CASCADE TEST 5246-2 -----	101
G.3.	CASCADE TEST 5329-2 -----	102
G.4.	CASCADE TEST 5330-2 -----	105

LIST OF FIGURES

1.	Transonic Compressor Cascade Apparatus -----	36
2.	Test Section Geometry -----	37
3.	Test Section Sidewalls -----	38
4.	Test Section Reference Coordinate System and Dimensions -----	40
5.	Instrumentation and Apparatus Layout -----	41
6.	View Toward the 96" Manometer Board -----	42
7.	Ramp-and-Drum Back Pressure Valve Assembly -----	43
8.	Back Pressure Valve Cutaway Showing Ramp Positions and Range of Drum Adjustment -----	44
9.	Porous Wall Bleed Control Valve -----	45
10.	Cascade Flow at -2.35° Incidence -----	46
11.	Cascade Flow at 0.91° Incidence -----	48
12.	Outflow Static Pressure Variation with Back Pressure Control Valve Setting -----	49
13.	Cascade Flow at 0.91° Incidence and Pressure Ratio of 1.07 -----	50
14.	Cascade Flow at 0.91° Incidence and Pressure Ratio of 1.51 -----	50
15.	Velocity Diagram Deduced from Measurements for the Cascade Blading at Minimum Loss Incidence -----	51
16.	Failed Aluminum Blade -----	52
17.	Test Section Following Failure of 1st Steel Blade --	54
18.	Flow Characteristics During and Subsequent to Steel Blade Failure -----	56
19.	Redesigned Cascade Blade Mount -----	58

A1.	Continuous Light Schlieren Source -----	64
A2.	Spark Light Source -----	65
A3.	Spark Source Installation -----	66
A4.	Light Source Selecting Mirror -----	67
A5.	Schlieren Knife Edge -----	68
A6.	Laser Alignment -----	69
B1.	Ramp Control Value -----	73
B2.	Ramp Actuator -----	74
B3.	Drum of Back Pressure Control Valve Showing Manual Actuator -----	75
C1.	Oscillation Measurement Apparatus Layout -----	79
C2.	Oscillation Sensor Housing -----	80
C3.	Pin Hole and Photodiode Installation -----	81
C4.	Oscillation Sensor Cutaway -----	82
E1.	Blade Passage Flow Calculation Model -----	92
E2.	Blade Pressure Loading Distribution -----	93

LIST OF SYMBOLS

English Letter Symbols

A	-	Flow area, in ²
C _{Di}	-	Induced drag coefficient
C _L	-	Lift coefficient
c	-	Chord, in
c _p	-	Specific heat at constant pressure (c _p = 0.24 Btu/lbm °R for air)
D	-	NASA diffusion coefficient
D*	-	Corrected diffusion coefficient
g _c	-	Proportionality factor (g _c = 32.174 lbm-ft/ lbf-sec in the English Engineering system of units)
h	-	Blade height, in
i	-	Incidence angle, degrees
K	-	Ratio of specific heats (K = 1.4 for air)
L	-	Lift, lbf
M	-	Mach number
\dot{m}	-	Mass flow rate, lbm/sec
P	-	Pressure, PSIA
q	-	Dynamic pressure, PSIA
s	-	Blade spacing, in
T	-	Temperature, °R
V	-	Velocity, ft/sec
W	-	Relative velocity, ft/sec
X	-	Dimensionless velocity ($X = V/\sqrt{2c_p T_t}$)

Greek Letter Symbols

β	-	Relative flow angle, degrees
α	-	Absolute flow angle, degrees
γ	-	Stagger angle, degrees
ϕ	-	Camber angle, degrees
δ°	-	Deviation angle, degrees
Δ	-	Finite difference
σ	-	Solidity
Ω	-	Wake momentum thickness parameter
$\tilde{\omega}$	-	Average total pressure loss coefficient
θ	-	Flow inclination angle behind oblique shock, degrees
δ	-	Flow deflection angle through oblique shock, degrees

Subscripts

0	-	Settling chamber
1	-	Blade row inlet
2	-	Blade row outlet
e	-	Exit
t	-	Total or stagnation
∞	-	Free stream

ACKNOWLEDGMENT

Sponsorship--The Naval Air Systems Command's research and exploratory development programs in Air-breathing propulsion, provided the motivation for and supported the equipment needs of the present study.

Support--The work presented here was made possible through the dedicated efforts of numerous individuals. Development of new data acquisition capabilities, cascade modification and testing could not have been accomplished without their knowledge and expertise. I'd like to thank Mr. Tom Polleck and Mr. Gil Liebfritz for coordinating the loan of NASA test equipment and patiently instructing me in its use.

Thanks to Mr. Alan McGuire for providing the continuity necessary in this on-going research effort and for his assistance in figure preparation. Thanks also to Mr. Jack King for his tutelage in optical data acquisition and help in sensor construction.

Special thanks go to Mr. Mike Odell, Mr. Ted Best and Mr. Blair Gammon. These three gifted individuals who fashion test equipment from ideas and odds and ends reclaimed from the scrap pile have literally built the framework for this investigation.

Special thanks also to Mr. Friedrich Neuhoﬀ and Dr. Atul Mathur who were always willing to drop what they were

doing and provide guidance on problems, procedures and interpretations.

Thanks to Professor R.P. Shreeve for furnishing the overall project direction and for his inspirational example of uncompromising dedication to meaningful research.

Most of all I'd like to thank my family for their sacrifices and unwavering support throughout the fatherless evenings and weekends.

I. INTRODUCTION

The work presented here reports and analyses data acquired from a blowdown transonic compressor cascade. An infinite cascade can be used to model the flow on a stream surface through a given blade row in an axial turbomachine. The two-dimensional geometry allows the use of measurement techniques not generally available in the rotating machine and greatly reduces the complexity of the required calculations. The present cascade apparatus is located in Building 230 at the NPS Turbopropulsion Laboratory (Figs. 1 and 2). The cascade was designed and built in 1978 [Ref. 1] to model the flow through the rotor tip section of the laboratory's single stage axial-flow transonic compressor. Operating in a blow-down configuration at a design upstream stagnation pressure of 50 PSIA produces a uniform two-dimensional flow at Mach 1.4 entering the blade row [Ref. 2]. Current air storage facilities provide 2 minute run times.

Modifications to the cascade prior to the present study enabled flow visualization by schlieren optics and variation of test section back pressure. A flow visualization capability was developed in the present study to augment pressure data in interpreting the flow structure in the cascade. The back pressure control was required to obtain a simulation of the compressor operating conditions with static pressure ratios of greater than 1.0 through the blade row [Ref. 2].

The experimental program reported here was aimed at understanding and documenting the flow behavior in the cascade in order to assist in the interpretation of the measurements obtained in the transonic compressor. Shock position and strength were of particular interest.

Varying static pressure ratios through the blade row from less than 1.0 to a maximum of 1.53 failed to produce the expected [Refs. 3,4,5] normal shock at the blade passage entrance. Increasing test section back pressure resulted in increased blade trailing edge oblique shock angles. The mass-averaged blade row exit Mach number was found to vary from a maximum of 1.56 with no back pressure control to a minimum of 1.02 at maximum back pressure.

Blade structural problems were manifested in fracture and cracking of the support tabs. The original aluminum blades were replaced with steel blades but these also experienced failures. Flutter is suspected as being the probable cause of the failures.

II. APPARATUS AND INSTRUMENTATION

A. GENERAL DESCRIPTION

The transonic cascade can be operated in two configurations. One system employs test section side walls of solid aluminum with 89 wall static pressure taps for data acquisition (Fig. 3a). This configuration was used in early testing and calibration studies [Ref. 2]. A second set of side walls with Plexiglas windows for flow visualization was built in 1983 [Ref. 6]. These windows permit observation of flow conditions in the three center blade passages (Fig. 3b). All of the results reported here were obtained using the windowed sidewalls.

Pressure data acquisition from the windowed sidewalls was limited to 18 wall static pressure taps, 12 of which were located downstream of the test section (Fig. 3b). Table 1 lists the locations of these static taps referenced to the coordinate system defined in Figure 4. Schlieren photographs and shadowgraphs provided the principal data for test runs with the tunnel in this configuration.

A single pass continuous light schlieren system [Ref. 7] was developed. A spark gap light source was obtained on loan from NASA Ames Research Center for shadowgraphs of unsteady or very high speed flow phenomenon. A diagram showing optical components and light paths for the two systems is

presented in Figure 5. Both systems employed common optics from mirror 1 (Fig. 5) to the camera/viewing screen. Photographs were taken with a Polaroid camera to document flow behavior. Details of the optical system design, setup and operation are given in Appendix A.

Pressure data from the test section was measured on a 96 inch Meriam mercury manometer referenced to atmospheric pressure (Fig. 6). The tubes were filled to 75 inches of mercury under static conditions to accommodate subatmospheric starting pressures as well as the nearly 2 atmospheres anticipated at the test section exit once test conditions were established. Mercury column heights were recorded photographically during the tests and the negatives were mounted as slides to be read manually for data reduction.

Upstream stagnation pressure was monitored on and read from a Heise absolute pressure gauge.

B. BACK PRESSURE CONTROL

Back pressure control was provided (for the first time) by a specially designed "ramp-and-drum" throttle valve located downstream of the test section (Fig. 7). After the flow was started through the test section the ramp was actuated by a pneumatic cylinder to the full up position (Fig. 8). Back pressure control was then obtained by steadily rotating the eccentrically mounted drum into the flow path reducing the exit gap. Minimum exit area for a given flow

condition gave the maximum back pressure attainable. The effects of back pressure variation on flow through the blade row were simultaneously monitored on the Schlieren system viewing screen and the manometer. Details of back pressure valve operation and adjustment are given in Appendix B.

C. POROUS WALL MASS FLOW CONTROL

Cancellation of wave reflections and alleviation of model blockage depended on the net flow allowed through the porous wall (Fig. 2) in the test section upper nozzle block [Refs. 2,3,8]. Wall bleed rate was controlled by restricting the exhaust from the small plenum located behind the porous wall. The porous wall exhaust control valve (Fig. 9) provided variable restriction of exhaust flow from fully closed (capped) to wide open (vented). Static pressure in the plenum exhaust was measured by a pipe-wall static tap. Total pressure at the exhaust exit was measured by a United Sensor KBC-12-W Kiel probe. These two pressures, on manometer tubes 19 and 20 respectively, were recorded photographically with test section pressure data.

The effects of varying porous wall bleed rate were monitored on the continuous light schlieren viewing screen.

D. CASCADE BLADES

The original cascade blades were machined from 7075-T6 aluminum and provided a factor of safety greater than three for the anticipated worst case steady state loads [Ref. 1].

Cracking and fractures in the blade mounting tabs during the present program of tests required the procurement of a new set of cascade blades. Preliminary failure analysis indicated the presence of torsional loading and fatigue not accounted for in the design. 4340 steel was therefore selected for a replacement set based on machining qualities, very high strength and resistance to fatigue. Table II provides a comparison between the mechanical properties of 4340 steel and 7075-T6 aluminum.

With the exception of the material, the replacement blades were similar to the original set. The blade retaining pins were also machined from 4340 steel and bonded to the tabs using Loctite 324 Speed Bond Adhesive.

E. OSCILLATION MEASUREMENT EQUIPMENT DESIGN

Equipment and procedures were developed for nonintrusive photo-optical measurement of very high speed flow oscillations. Flow phenomena of interest included bow shock wave oscillations and blade trailing edge vortex shedding. The technique centered on a very sensitive, high frequency response photodiode which was to be illuminated through the test section by the continuous light schlieren source. Proper positioning of the photodiode behind a pin-hole aperture would cause it to be covered and uncovered by the oscillating flow, producing an output which could be monitored on an oscilloscope or frequency analyzer. Details of the

equipment design are provided in Appendix C. Failure of the second blade set prevented use of the equipment.

III. EXPERIMENTAL PROGRAM AND PROCEDURES

A. PRELIMINARY TESTS

Initial testing was performed to determine the structural integrity and behavior of new components. The tests were conducted with the blade pressure surfaces (bottoms) aligned with the tunnel axis and the porous wall bleed rate unrestricted, as had been the case in previous tests [Ref. 2]. Throttle valve operation and integrity were verified and the sequencing of throttling procedures was established. Back pressures attained during this phase were lower than those of practical interest. Manometer response was checked for sensitivity and tendency to overshoot during rapid pressure changes. Only four static taps were connected, two upstream and two downstream of the test section. The pressure tap plumbing was adjusted to provide rapid, sensitive response with acceptable overshoot characteristics. The Schlieren system was set up and optimized during this phase of testing.

B. BACK PRESSURE VARIATION AND WAVE CANCELLATION: PHASE 1

A series of tests at increasing back pressure were conducted next in order to attain the expected design run condition with a normal shock at the blade passage entrance. The blade pressure surfaces remained aligned with the tunnel axis. Since the manometer behaved well at higher pressures the remaining pressure taps were connected.

The porous wall bleed rate was adjusted at each new back pressure. The exhaust from the porous wall plenum was restricted to the maximum extent possible without precipitating unstating of the test section due to blockage effects. Starting of the test section at plenum design operating conditions with a partially restricted porous wall bleed rate was also verified. The series of tests was terminated when cracking and multiple fractures were discovered in the aluminum blade retaining tabs.

Data from two test runs in phase 1 are reported in Chapter IV.

C. BACK PRESSURE VARIATION AND WAVE CANCELLATION: PHASE 2

Test runs were made with new steel blades installed and set with the pressure surfaces rotated to 3.26° angle of attack with respect to the tunnel axis. This setting corresponded to the minimum loss incidence angle of 0.91° as defined in Chapter 6 of Reference 9 and gave the set of parameters listed in Table III. Testing was continued at increasing back pressures in an attempt to attain a subsonic blade row exit Mach number and normal shock at blade passage entrance. The porous wall bleed rate was adjusted as before to ensure correct mass flow through the throttle valve. The tests were terminated when the leading (farthest upstream) blade experienced failures in all four blade retaining tabs.

Data from two test runs in phase 2 are reported in Chapter IV.

D. TEST PROCEDURES

The general procedures followed in all test runs were similar to those employed in previous investigations [Ref. 2] and are presented in detail in Appendix D. Flow through the tunnel was started and controlled by the supply control valve. When the test section had started and design supply pressure had been established stably, the ramp was actuated. Back pressure was then adjusted by rotating the eccentric drum. The test conditions were monitored on the continuous light Schlieren viewing screen and from the manometer. Manometer pressures were recorded photographically for desired test conditions. Schlieren photographs were taken as required.

The test run was terminated when the desired data had been obtained or when the supply pressure dropped below 50 PSIA.

IV. RESULTS AND DISCUSSION

A. GENERAL FLOW CHARACTERISTICS

1. Shock Patterns

Continuous light Schlieren photographs of cascade flow at blade incidences of -2.35° and 0.91° are shown in Figures 10 and 11 respectively. The Mach waves shown emanating from the upper nozzle block are generated by flow interaction with holes in the porous wall. Bow shocks in both figures show very little curvature indicating that interactions with Mach waves do not significantly alter the shock strength.

Bending of shock waves near the upper nozzle wall surface is attributed to the presence of a transverse pressure gradient in close proximity to the wall [Ref. 10]. The porous wall produces a decrease in pressure which causes the streamlines to bend outward, producing the shock curvature.

Blade row exit velocities are clearly supersonic in Figure 10 as indicated by the trailing edge oblique shocks and expansions. Photos in Figure 10 correspond to a static pressure ratio through the blade row of 1.006. The average turning angle was found graphically to be approximately 4° .

In Figure 11 the oblique shocks are much stronger but exit velocities are still supersonic. The corresponding pressure ratio was 1.51 and average turning angle 6° .

2. Periodicity

Bow shock angles for five blades were measured from schlieren photographs and found to be parallel to within $\pm 3^\circ$ for a given test run. The largest variations involved the first shock originating from the lower boundary layer scoop. Tunnel disassembly following the tests revealed that the right corner of the scoop leading edge was bent down slightly. This bend is likely to have contributed to the difference in the first shock wave angle. Measurement uncertainty for the angles was $\pm 2^\circ$ principally due to shock width on the continuous light photos. Losses through the shocks were calculated to be very small (Appendix E) except near the blade leading edges where the shocks were normal. Turning of the streamlines by upstream shocks was found to be approximately compensated for by flow expansion over the suction surface prior to encountering the next blade. Approaching Mach numbers calculated from measured shock angles were found to be equal from shock to shock to within the uncertainty in the shock angle measurement.

Small differences in flow structure through the two center blade passages can be seen in Figures 10 and 11. The differences involve slightly different shock impingement points on the suction surface of the lower blade in each passage, and consequently differences in the impingement of the reflected shocks on the pressure surfaces at the top of each passage. It is noted that at $M = 1.4$, a change in shock

angle of 1° results from a change in flow angle of only $1/2^\circ$. Consequently the differences which are seen imply relatively small departures from periodicity.

3. Back Pressure Variation

The back pressure was varied at two different blade incidences. The highest static pressure ratio achieved through the blade row at -2.35° was 1.05. Changing incidence to 0.91° increased the turning through the blade row and produced a static pressure ratio of 1.24 at the same throttle setting. Maximum static pressure ratio achieved at 0.91° incidence was 1.53.

Figure 12 shows an example of the variation in outlet static pressure during a test run. Blade row static pressure ratios varied from 0.78 to 1.51 for the data in this figure. Schlieren photographs corresponding to conditions 2 and 6 of Figure 12 are shown in Figures 13 and 14 respectively.

Increasing back pressure caused the trailing edge oblique shocks to bend farther upstream, increasing in strength (Fig. 14) and reducing blade row exit velocity.

Large rapid increases in back pressure (ramp actuation) caused bow shocks to momentarily increase in angle (become more normal). Repeated observation of this behavior prompted questions concerning upstream propagation of pressure disturbances in a supersonic flow. Prince [Ref. 12] documents other cases of similar behavior and cites pressure transmission

through corner boundary layers between airfoil surfaces and tunnel sidewalls as the likely mechanism.

B. WAVE CANCELLATION

Cancellation of reflected waves was found to occur independent of porous wall mass flow control. Mass flow control was effective in minimizing the strength of the Mach waves generated by the porous wall (contrast Figures 10a with 10b and 11a with 11b for example). Optimum wall bleed rate was found to be a function of blade incidence and test section back pressure. Figure 10c illustrates partial test section unstating caused by excessive restriction of the porous wall mass flow. The porous wall provides compensation for test section physical and viscous blockage in addition to wave cancellation. Unstarting in Figure 10c was attributed to restriction of porous wall bleed to the point where insufficient blockage compensation was provided.

Increasing blade incidence to 0.91° allowed complete closure of the porous wall bleed control without producing unstarting (Fig. 11b).

C. CASCADE DESIGN AND PERFORMANCE

Blade row design inlet conditions in phase 2 were set as calculated in Reference 1 following Chapter 6 of Reference 9. Minimum loss incidence angle determined the design point. This angle corresponded closely to the incidence recommended for blading with supersonic relative inlet Mach number in

Reference 11. The steel blades were set to the design incidence condition when first installed.

Inaccuracies in the design calculations for the transonic compressor blading [Ref. 5] being modeled by the present cascade resulted in insufficient information being available to specify, with certainty, the design blade row exit conditions. Near sonic exit velocity was anticipated with a pressure ratio through the blading of approximately 1.5. Performance calculations at maximum back pressure (Appendix E) gave a pressure ratio of 1.53 and mass averaged exit Mach number of 1.02. However, the predicted normal shock at the blade passage entrance was not present at this test condition. A velocity diagram depicting design inlet and maximum back pressure exit conditions is shown to scale in Figure 15.

Losses calculated using the flow model in Appendix E reflect only the shock losses. "Design" calculations in Appendix F account for profile, secondary flow and shock losses. There the shock losses were calculated using the method of Wennerstrom [Ref. 13]: however it is noted that this model is based on a normal shock occurring at the blade passage entrance and, in fact, only oblique shocks were found to be present. A summary of profile, secondary flow and shock loss calculations based on the blading geometry and test parameters is contained in Appendix F. The total loss coefficient obtained for the full blade in the present cascade at design conditions was 0.145.

D. BLADE FAILURES

Failure of the blade mounting tabs occurred in both aluminum and steel blades. The initial failures (aluminum blades) were detected between tests while realigning the optical system when a sharp focus on blade leading and trailing edges could not be obtained. Wear marks on the Plexiglas sidewalls adjacent to the fractured tabs were the only additional damage. Fracture occurred in 3 of 4 tabs on the number 1 (farthest upstream) blade (Fig. 16a). The number 2 blade exhibited 1 fracture (Fig. 16b). Extensive cracking was found in the vicinity of most tabs on these blades [Ref. 14] and also on the number 3 blade. The exact number of tests conducted prior to failure is not known. Reference 2 reports fourteen tests conducted but blades were not installed for all tests. Seven additional tests were conducted in this investigation prior to blade failure.

Examination of the cracked aluminum blades revealed fractures seemingly due to twisting that didn't occur at the tab bases (Fig. 16a) where the sharp corners created stress concentrations. Torque applied to retaining screws intended to provide air seals to prevent them from vibrating loose during tests, and fatigue associated with test section vibration, were considered to be the most probable causes. Reference 14 gives a detailed analysis of the failure of the aluminum blades.

Failure of the aluminum blades led to a search for a better material. Graphite epoxy composite blades were considered briefly for their high fatigue resistance, but were rejected because of the serious difficulty in meeting the surface finish specification. Heat treated 4340 steel was selected based on very high strength, excellent fatigue resistance and good machining qualities.

Reexamination of test conditions used in phase 1 revealed an inconsistency in the marking of the scale for rotation of the test section. Selecting 0° on the test section sidewall rotational scale actually corresponded to -2.35° incidence. This was considered to be an adverse run condition. Subsequent testing was therefore conducted at design incidence.

After six successful test runs with the steel blades installed, failure of all 4 blade retaining tabs during run seven, resulted in the loss of the number 1 blade from the test section (Fig. 17). The aft tabs appear to have failed first since a wide arced scratch was generated on the left sidewall near the trailing edge, presumably before the blade was completely free (Fig. 17a). The blade leading edge also flexed down gouging the right aft section of the lower boundary layer scoop (Fig. 17b). Several other gouges were inflicted in the sidewalls as the blade made its way out of the test section. The throttle valve and exhaust duct were free of damage.

Figure 18 shows a series of Schlieren photographs taken during the failure. The blade is still present in Figure 18a but is missing in subsequent photos. Flow breakdown caused by the missing blade is evident in Figures 18c and 18d.

A comprehensive failure analysis of the steel blade is in progress. Steady loads calculated from both deduced pressure distributions (Appendix E) and blade design assumptions (Appendix F) are well below the load carrying capability of the tabs. Fracture of the steel blade did occur at the tab base but evidence of twisting was still present. No air seal (retaining) screws were used with the steel blades eliminating the possibility of mechanical torque being unintentionally applied to the blade tabs.

Fatigue is suspected as being ultimately the mechanism of blade failure. Test section vibration was noted on all test runs but quantitative investigation of frequency and amplitude was not attempted. It appears that the blades may have encountered a flutter condition at the higher back pressures.

V. CONCLUSIONS AND RECOMMENDATIONS

Experimentally acceptable flow periodicity was verified by schlieren photographs and downstream static pressure distributions for a wide range of back pressures (pressure ratios from 0.78 to 1.53). Small deviations that were noted can be reduced by straightening the leading edge of the lower boundary layer scoop. Thus this small (but effectively "infinite") cascade model can serve as a tool for gaining insight into the complex transonic compressor rotor flow field characteristics.

The maximum back pressure test condition at minimum loss incidence closely reproduced the design pressure ratio and exit Mach number documented in the transonic compressor design notes. Large discrepancies were found however between design and cascade measurements of turning angle through the blade row and shock structure. Design calculations predicted a turning at the tip of 0.58° and a normal shock was expected to appear in each blade passage. Cascade data showed a fully oblique shock structure and an average turning of 6.8° was measured from Schlieren photographs.

The cascade performance calculations carried out were preliminary and require many approximations and assumptions. The validity of the calculative model can be tested by static pressure measurements through the blade row and downstream measurements of flow angle and total pressure.

The throttle valve provided an effective means of varying and controlling back pressure. The precise positioning provided by drum rotation allowed reproducible uniform downstream pressure boundary conditions to be controlled as necessary for simulation of actual compressor blade row conditions.

Integrity of the components of the apparatus was also verified over a wide back pressure range. The blades were the only components to experience failures. A full understanding of the blade failure mechanism will require further testing to ascertain blade fundamental frequencies, test section vibration characteristics and cascade aerodynamic flutter boundaries.

Recommended modifications to the apparatus include the following:

1. Incorporation of a probe for total pressure and flow angle measurement downstream of the test section. Traversing mechanism requirements include sidewall to sidewall movement at various points downstream of the cascade exit plane. Installation difficulties could be minimized by incorporating this instrumentation in the solid aluminum sidewalls.
2. Blade retaining tab redesign would provide an alternative to extensive flutter investigations. A single continuous tab on each side of the blade (Fig. 19) faired at the base to reduce stress concentrations would provide a 200% increase in load carrying area. These tabs would fit into slots in the test section sidewalls. This design also allows elimination of the round mounting pins which obscure flow visualization over parts of the blade surfaces.

If the blade structural problem is solved cascade investigations should be aimed at acquiring the following data for the current maximum back pressure test condition:

1. Blade row static pressure distributions
2. Total pressure losses through the blade row
3. Flow turning angle
4. Documentation of unsteady phenomena using spark shadowgraphs and high speed electro-optical equipment.

TABLE I
PLEXIGLAS SIDEWALL STATIC PRESSURE TAP LOCATIONS

STATIC PRESSURE TAP COORDINATES

Left Sidewall

Pressure Tap No. 1	X = -4.500	Y = 0.075
Pressure Tap No. 3	X = 0.000	Y = -4.500
Pressure Tap No. 5	X = 4.500	Y = 0.075
Pressure Tap No. 7	X = 7.600	Y = 3.870
Pressure Tap No. 9	X = 7.600	Y = 1.870
Pressure Tap No. 11	X = 7.600	Y = -0.130
Pressure Tap No. 13	X = 7.600	Y = -2.130
Pressure Tap No. 15	X = 7.600	Y = -4.130
Pressure Tap No. 17	X = 7.600	Y = -6.130

Right Sidewall

Pressure Tap No. 2	X = -4.500	Y = 0.075
Pressure Tap No. 4	X = 0.000	Y = -4.500
Pressure Tap No. 6	X = 4.500	Y = 0.075
Pressure Tap No. 8	X = 7.600	Y = 3.870
Pressure Tap No. 10	X = 7.600	Y = 1.870
Pressure Tap No. 12	X = 7.600	Y = -0.130
Pressure Tap No. 14	X = 7.600	Y = -2.130
Pressure Tap No. 16	X = 7.600	Y = -4.130
Pressure Tap No. 18	X = 7.600	Y = -6.130

TABLE II

MECHANICAL PROPERTIES OF 7075-T6 ALUMINUM AND 4340 STEEL

	<u>7075-T6</u>	<u>4340</u>
yield strength	73 KSI	200 KSI
tensile strenth	83 KSI	211 KSI
% elongation	11	10
Brinell hardness	60	426

TABLE III

CASCADE BLADING DESIGN PARAMETERS

Stagger Angle (γ):	59.743°
Camber Angle (ϕ):	4.7°
Solidity (σ):	1.4
Blade Chord (c):	1.882 in
Air Inlet Angle (β_1):	63.0°
Minimum Loss Incidence Angle (i):	0.91°
Deviation Angle (δ°):	1.39°
Turning Angle ($\Delta\beta$):	4.25°

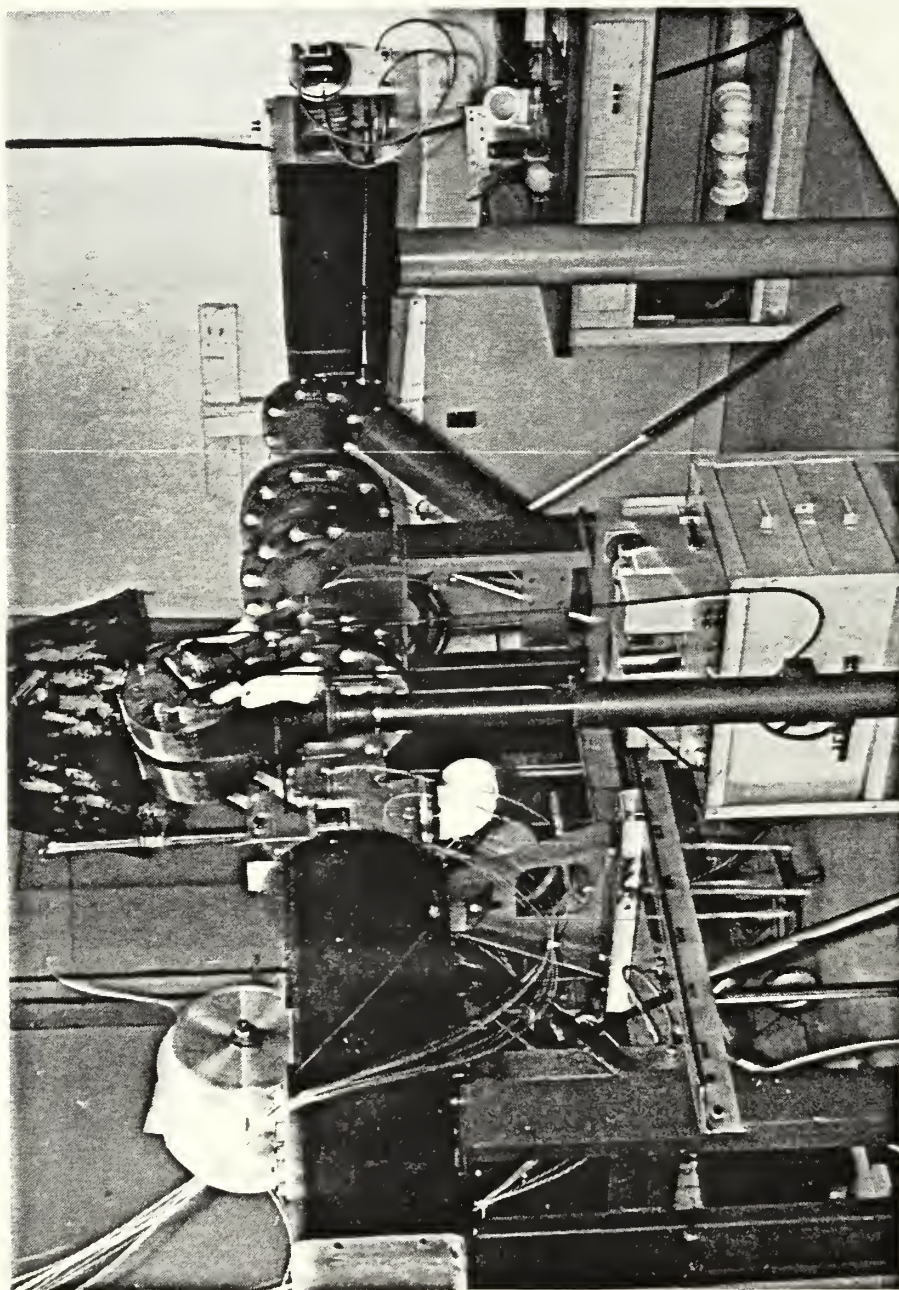


Figure 1. Transonic Compressor Cascade Apparatus

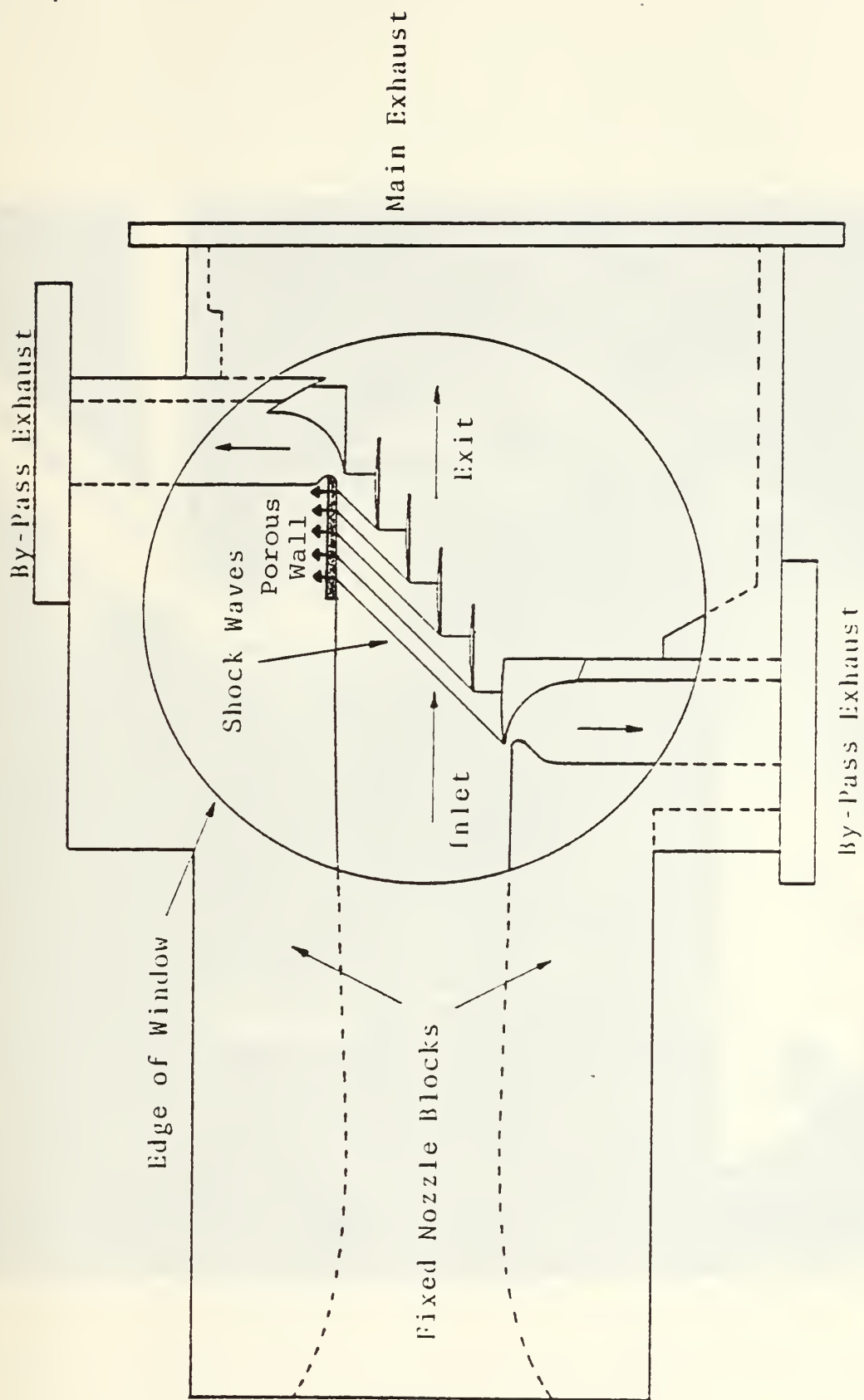
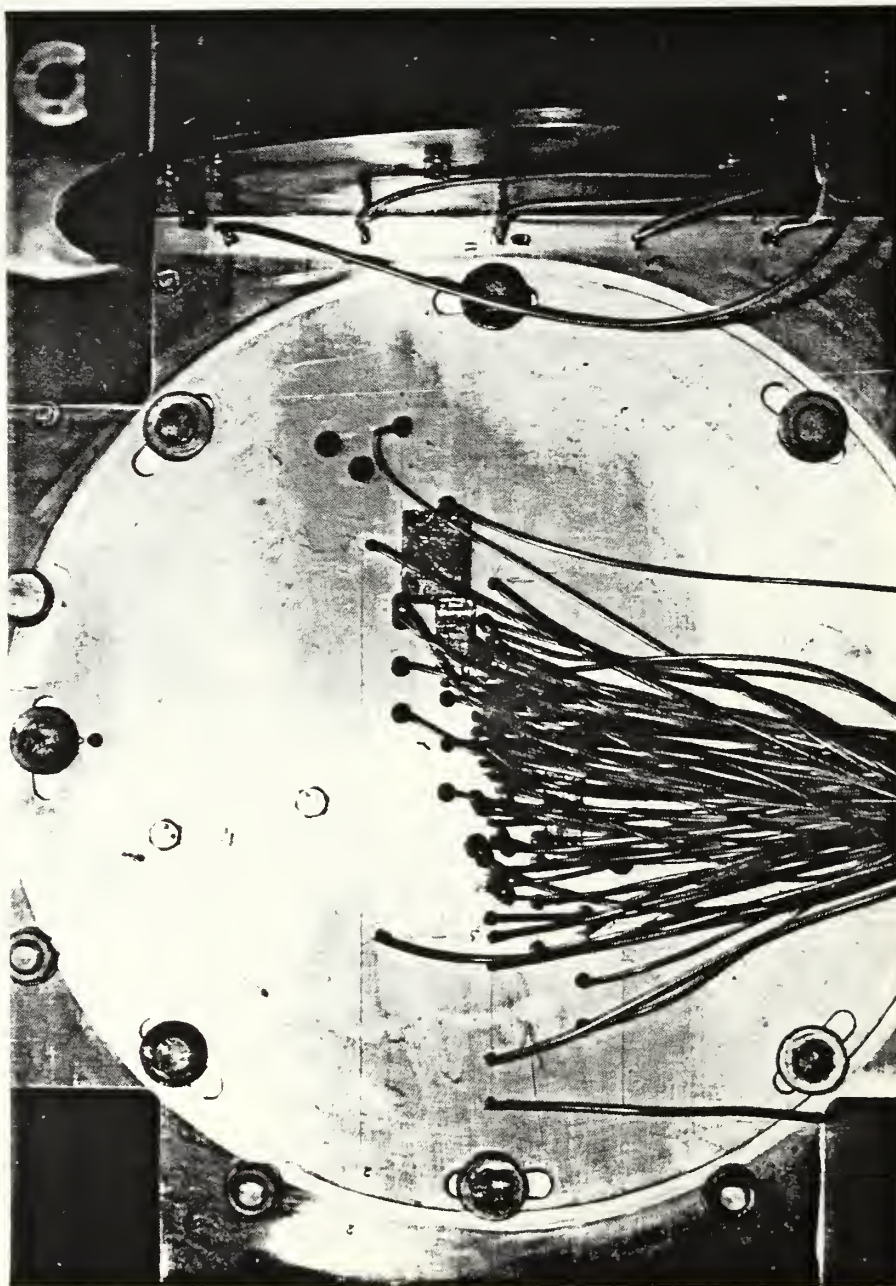
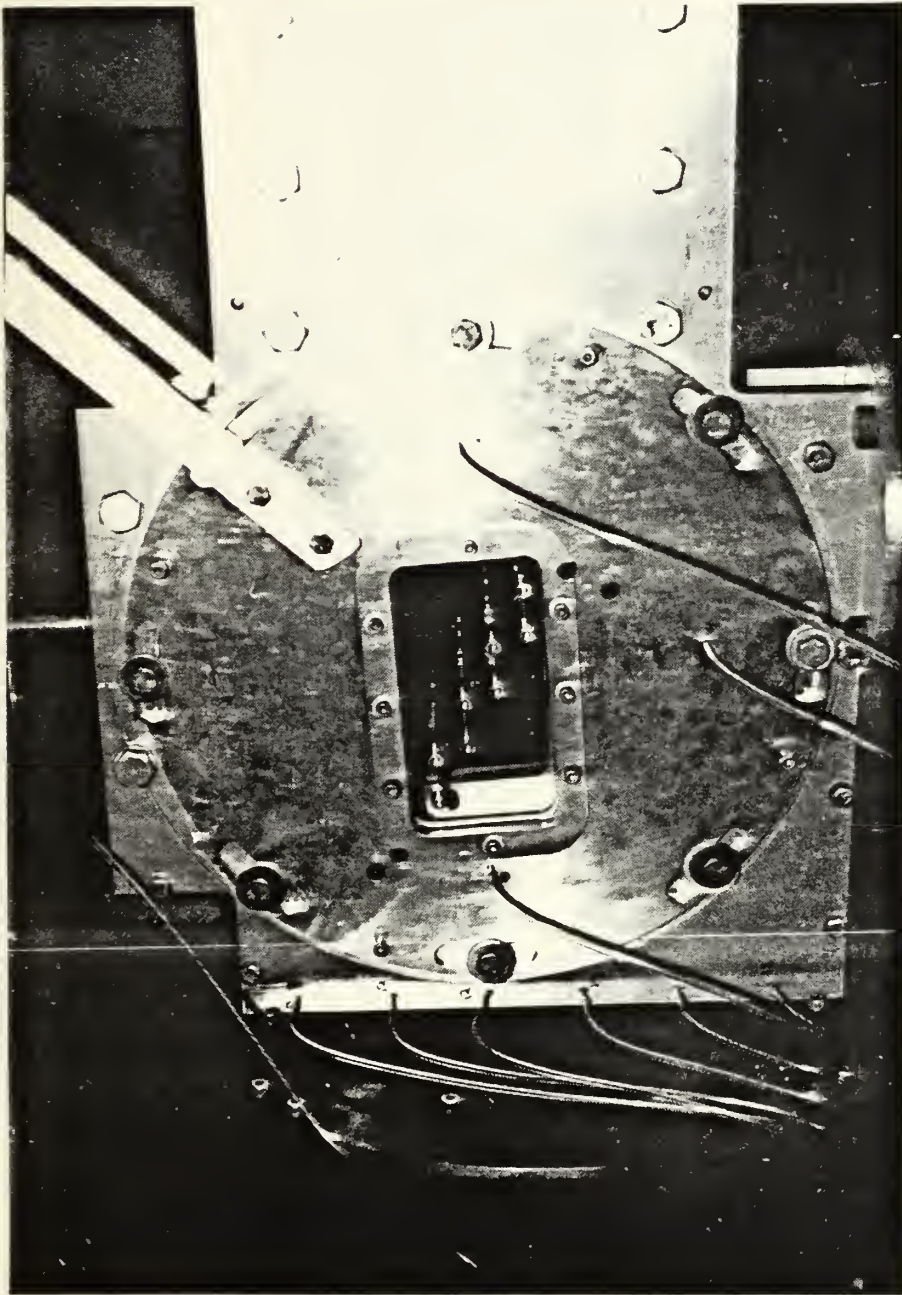


Figure 2. Test Section Geometry



a. With Pressure Taps

Figure 3. Test Section Sidewalls



b. With Windows

Figure 3. (CONTINUED)

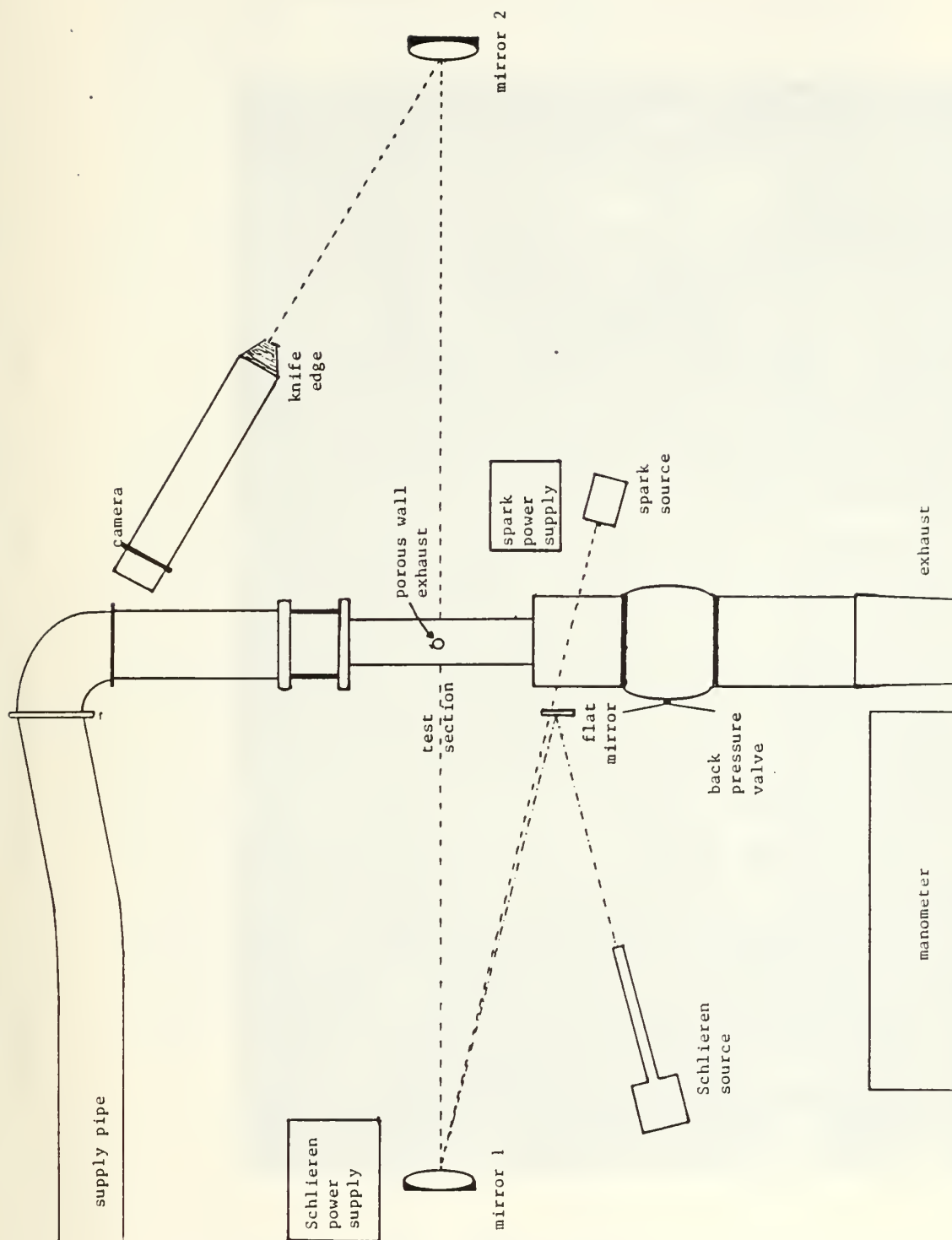


Figure 5. Instrumentation and Apparatus Layout

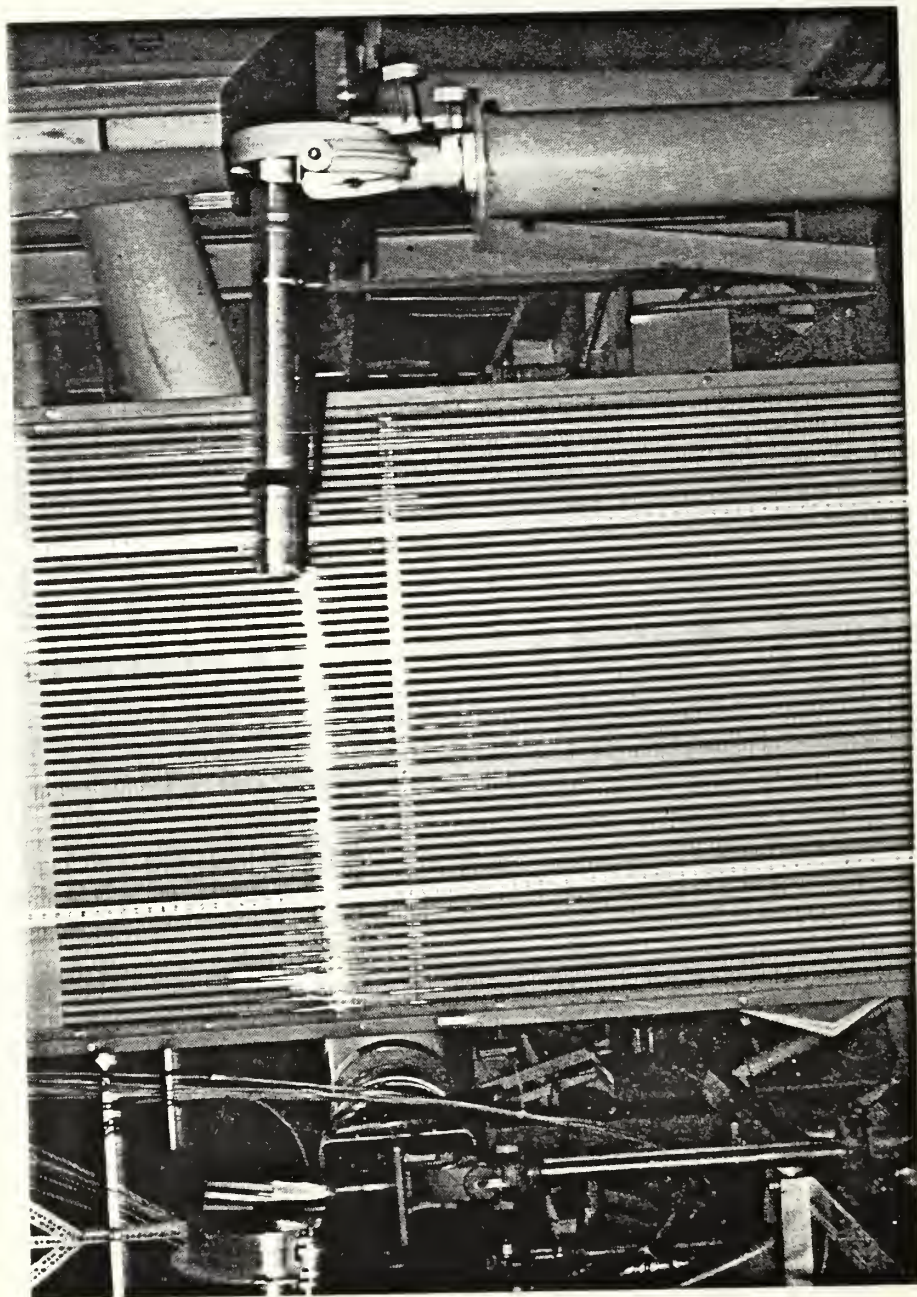


Figure 6. View Toward the 96" Manometer Board

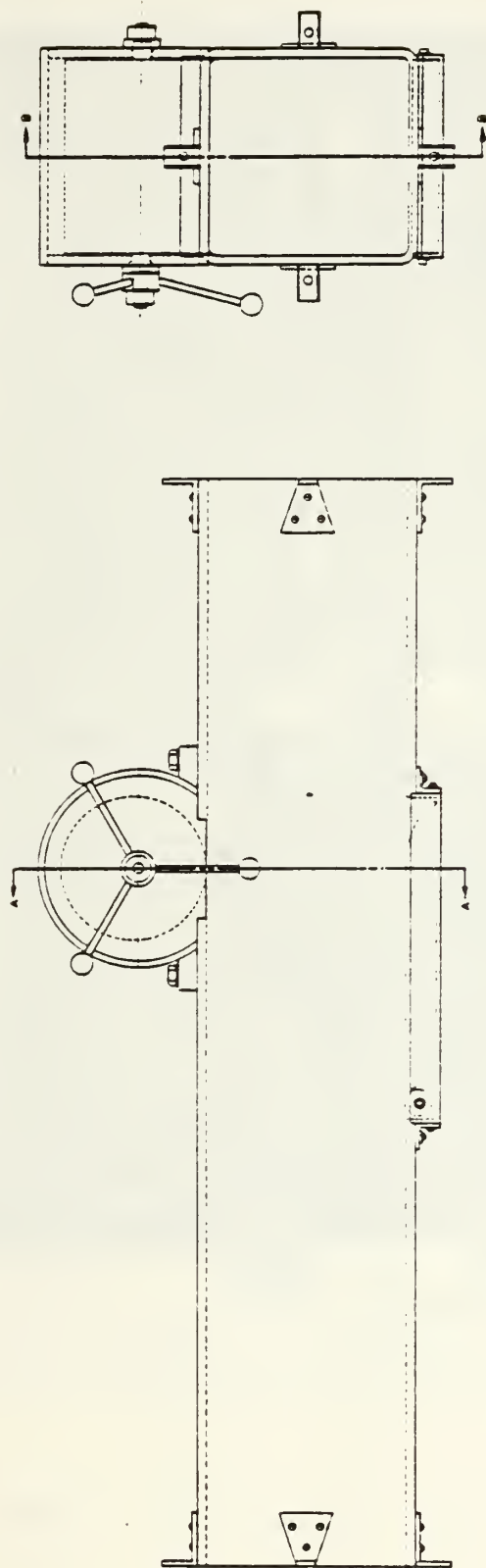


Figure 7. Ramp-and-Drum Back Pressure Valve Assembly

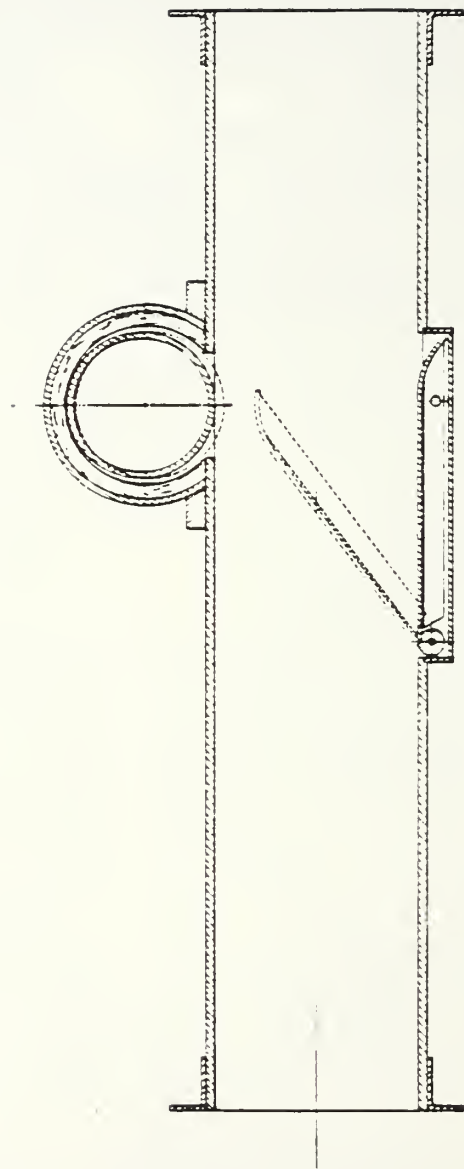


Figure 8. Back Pressure Valve Cutaway Showing Ramp Positions and Range of Drum Adjustment

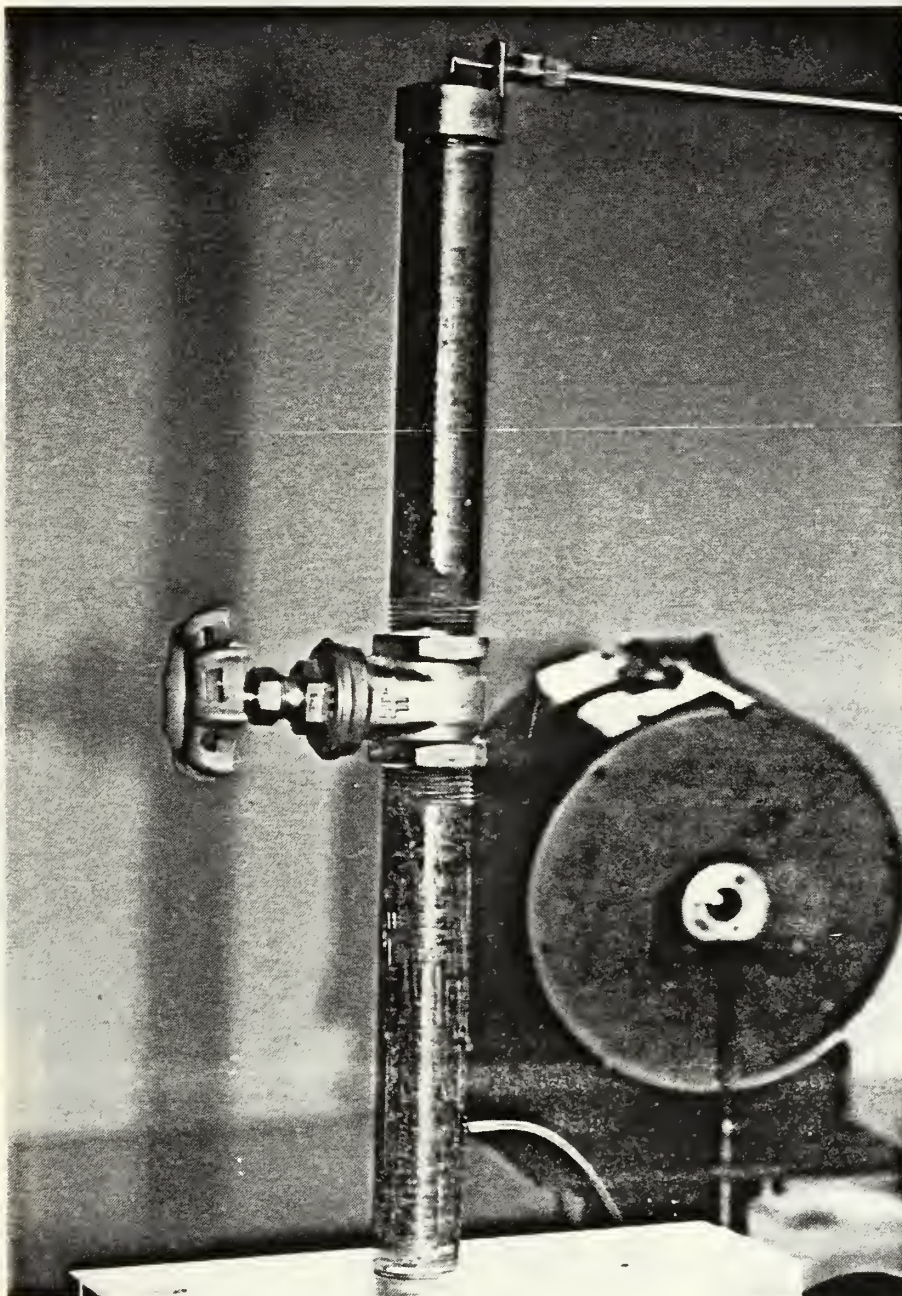
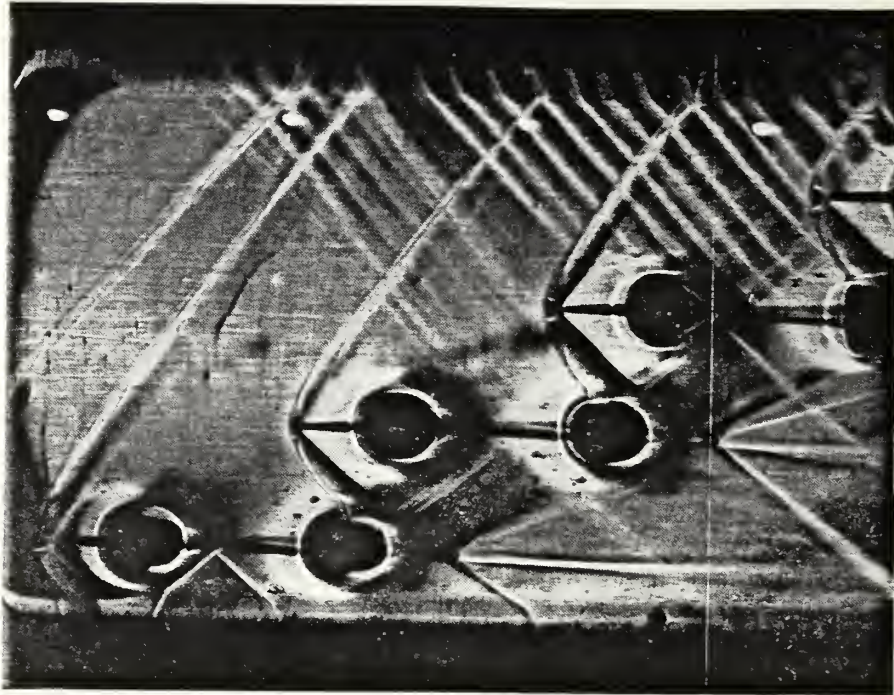
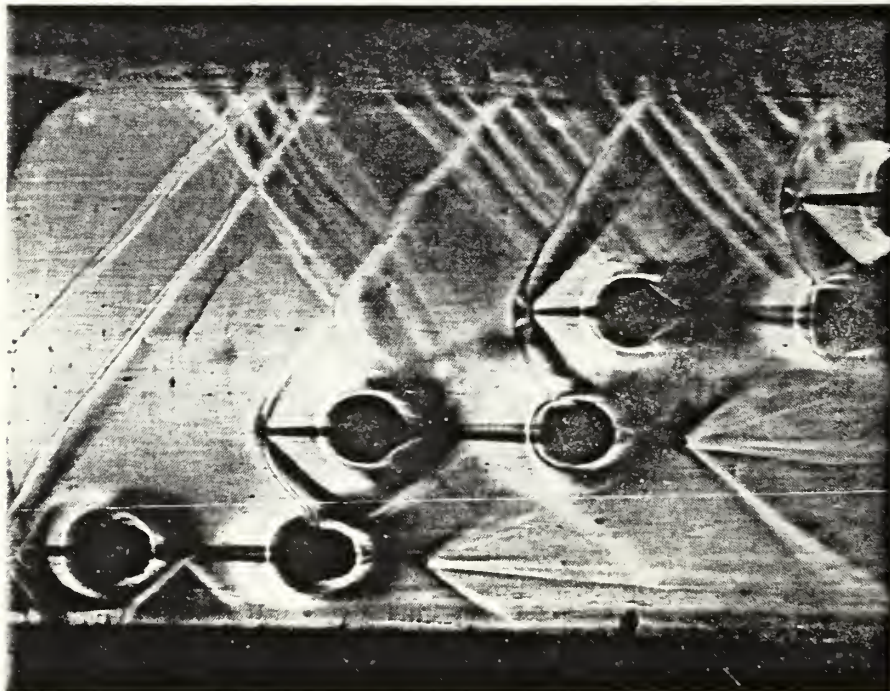


Figure 9. Porous Wall Bleed Control Valve

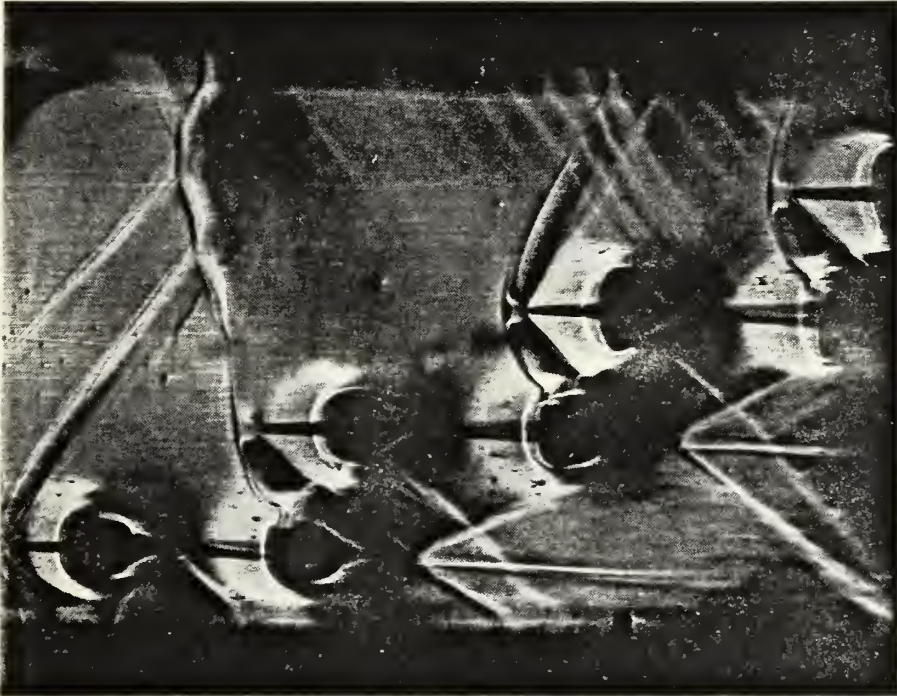


a. Unrestricted Porous Wall Bleed



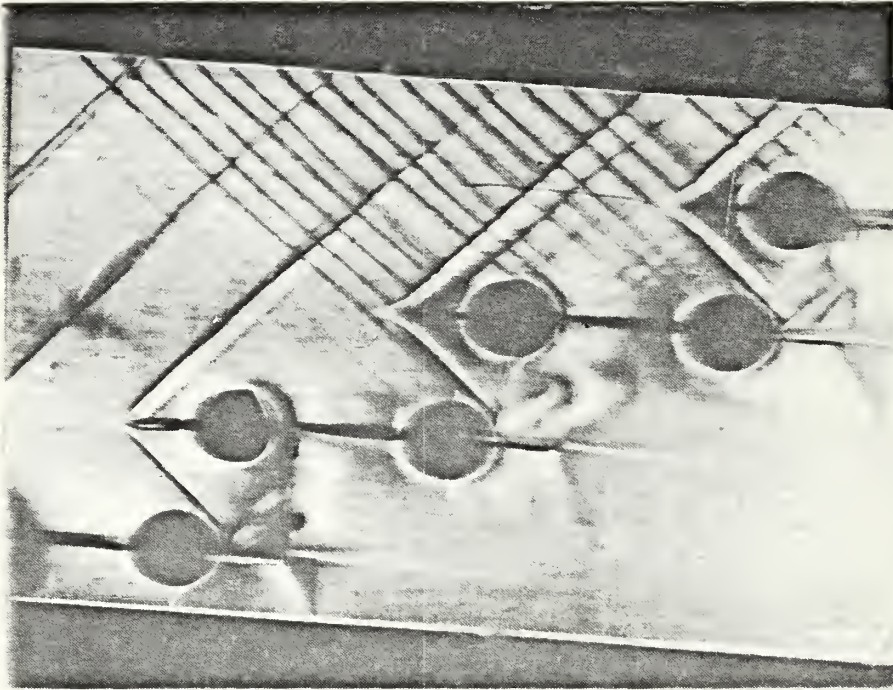
b. Optimum Porous Wall Bleed

Figure 10. Cascade Flow at -2.35° Incidence



c. Excessive Porous Wall Bleed

Figure 10. (CONTINUED)



a. Unrestricted Porous Wall Bleed



b. Optimum Porous Wall Bleed

Figure 11. Cascade Flow at 0.91° Incidence



Figure 12. Outflow Static Pressure Variation with Back Pressure
Control Valve Setting (1. Ramp Down, 0% Drum; 2. Ramp
Up, 0% Drum; (3-6). Increasing Drum Displacement)

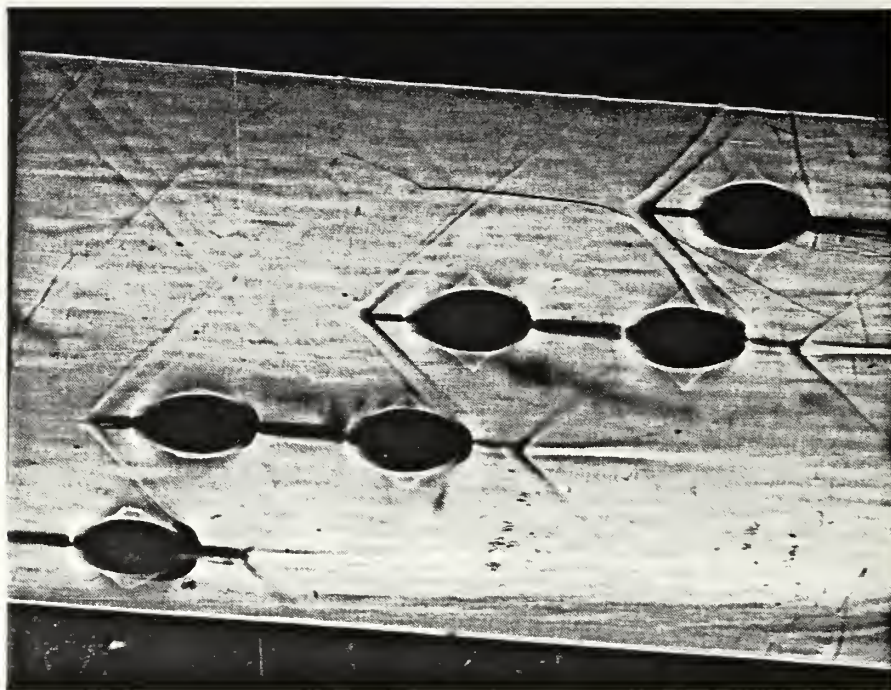


Figure 13. Cascade Flow at 0.91° Incidence and Pressure Ratio of 1.07

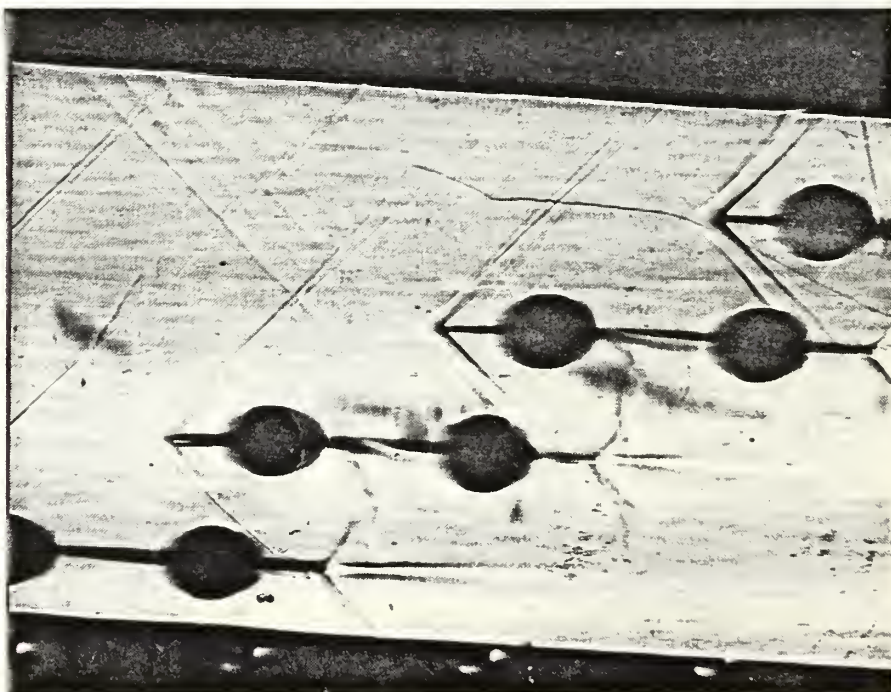


Figure 14. Cascade Flow at 0.91° Incidence and Pressure Ratio of 1.51

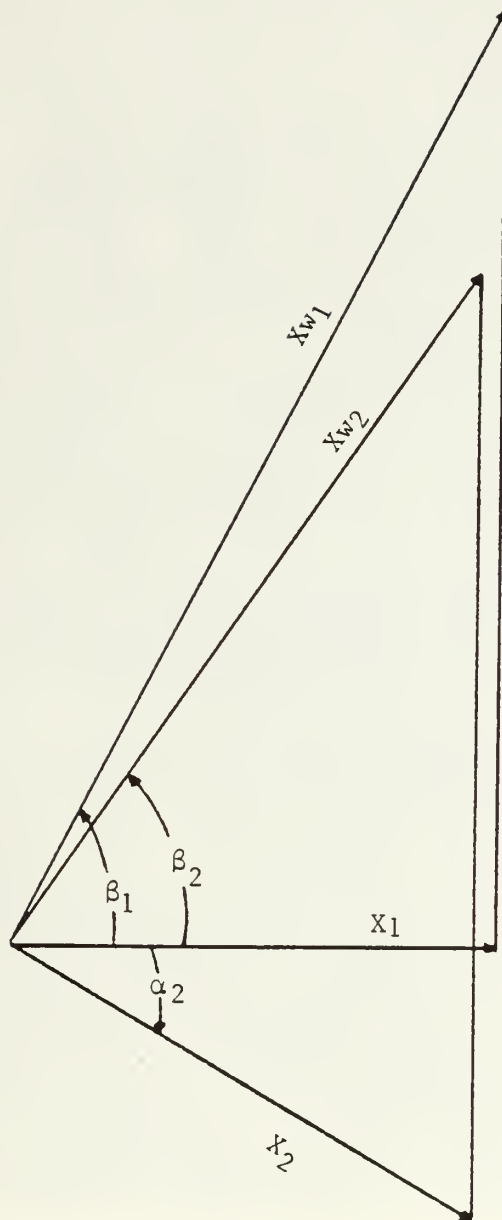
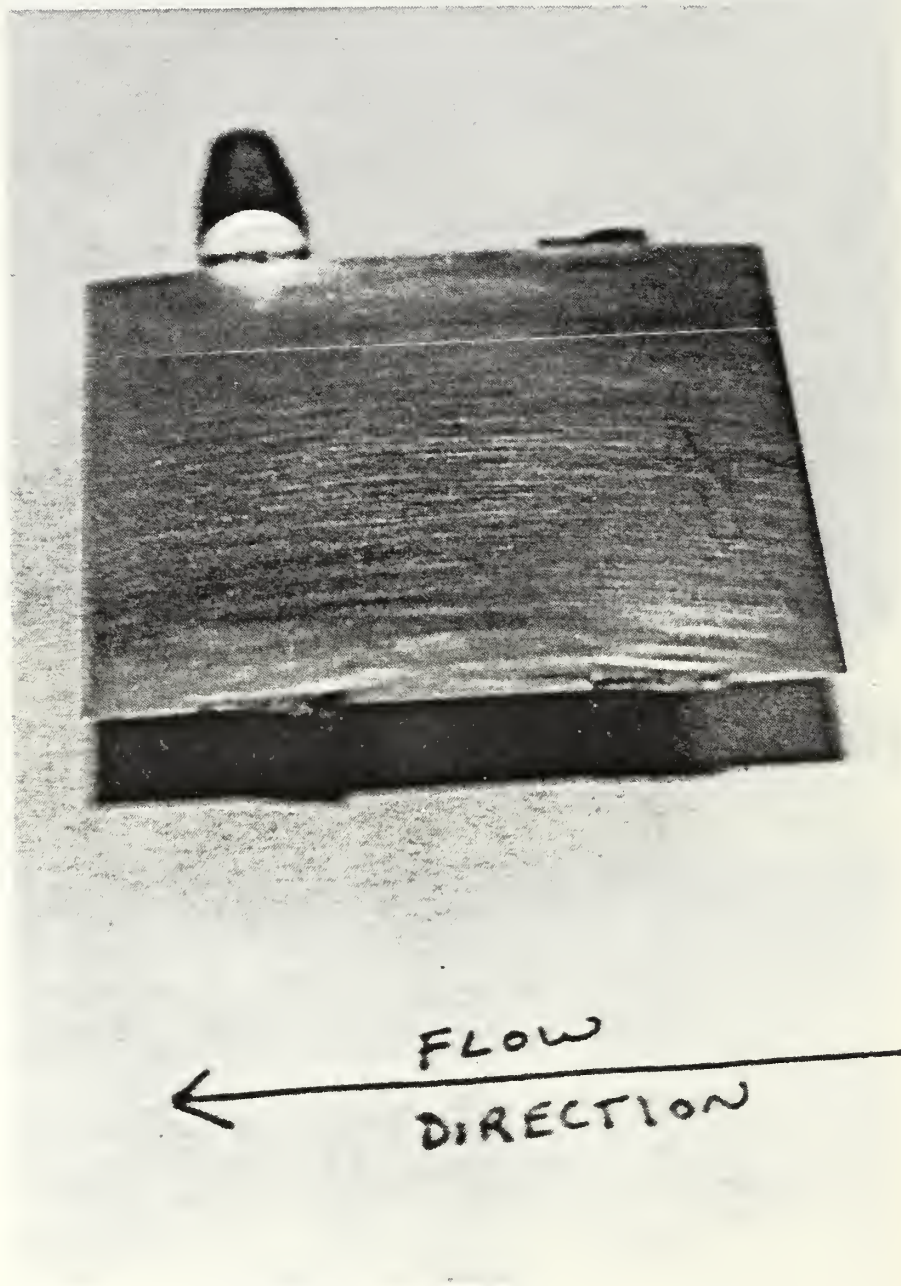
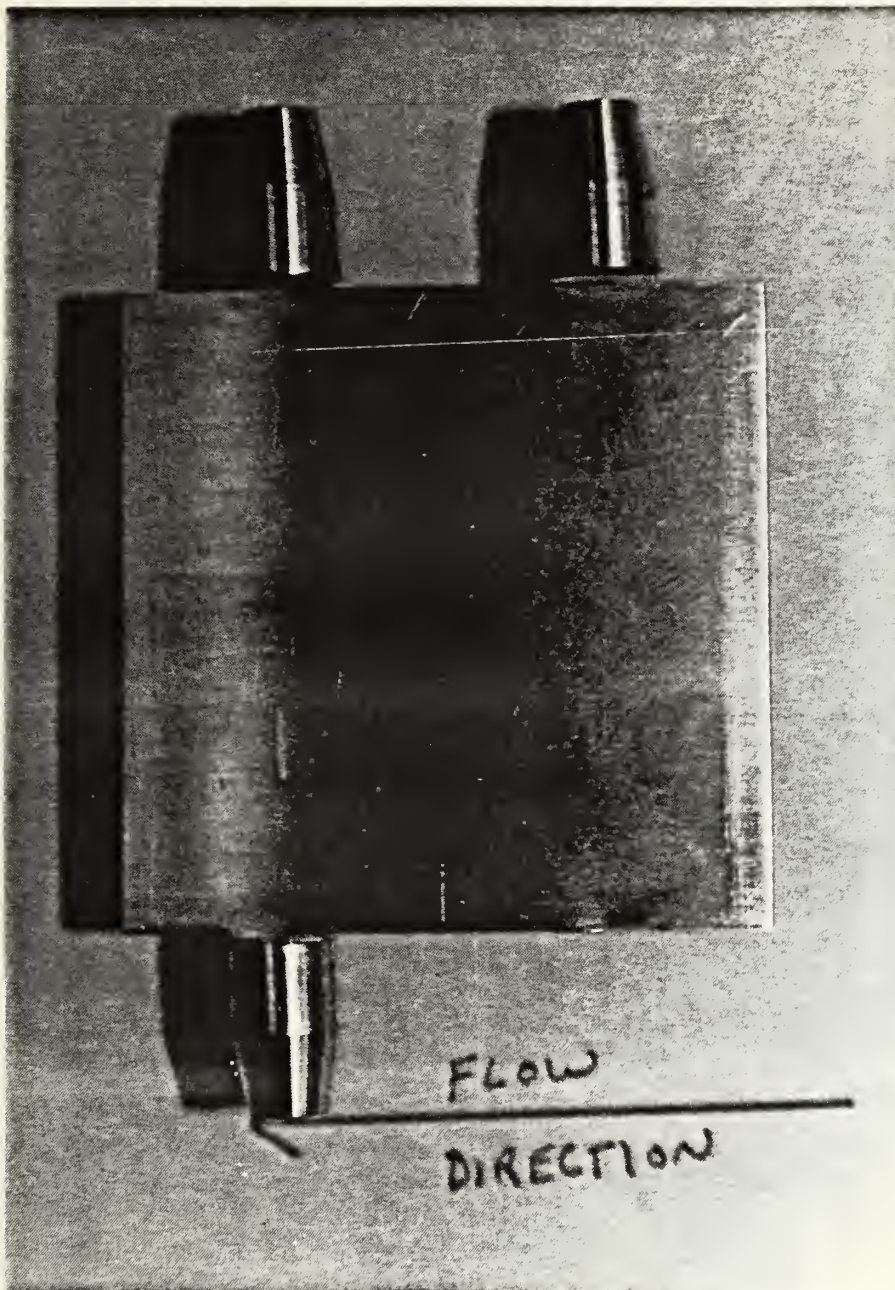


Figure 15. Velocity Diagram Deduced from Measurements for the Cascade at Minimum Loss Incidence



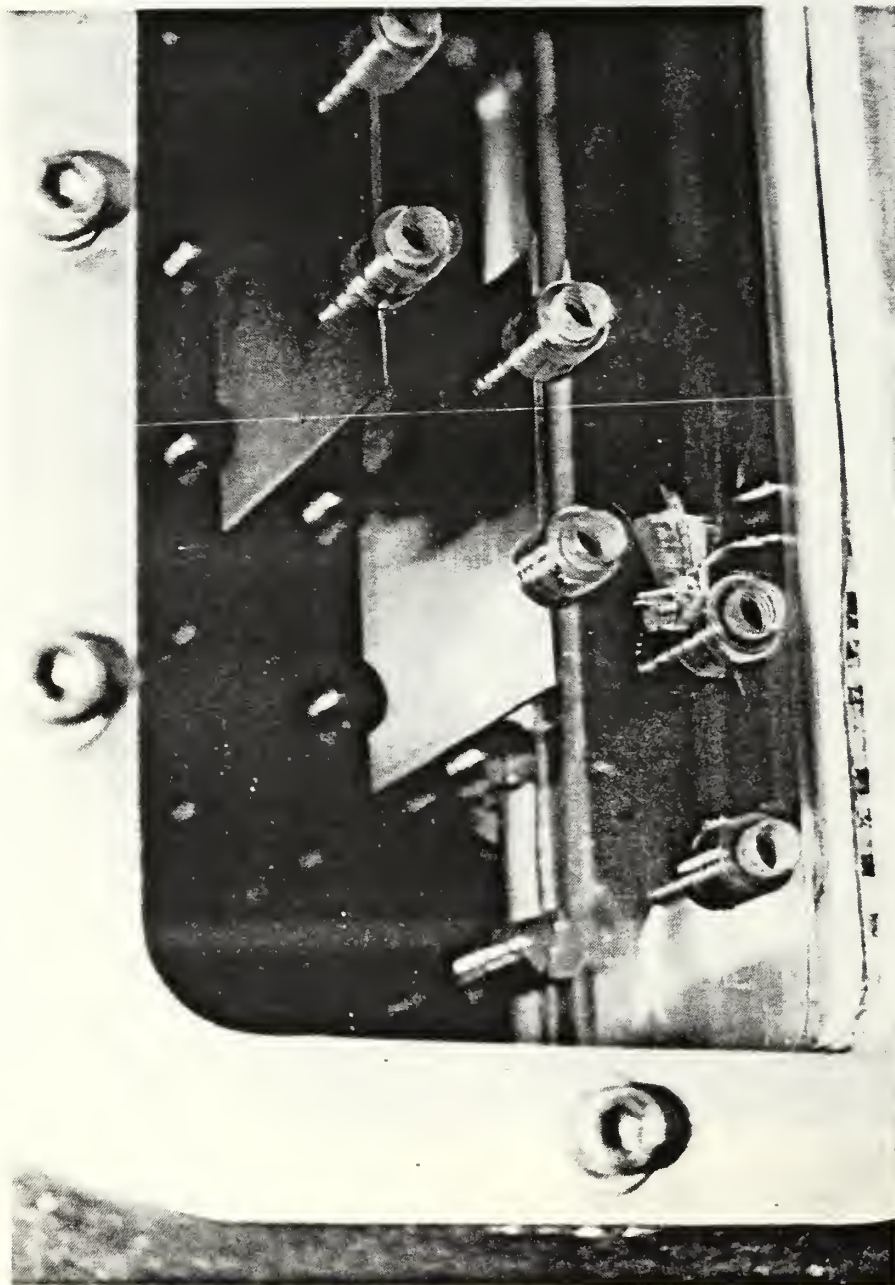
a. 1st Blade from Upstream

Figure 16. Failed Aluminum Blade



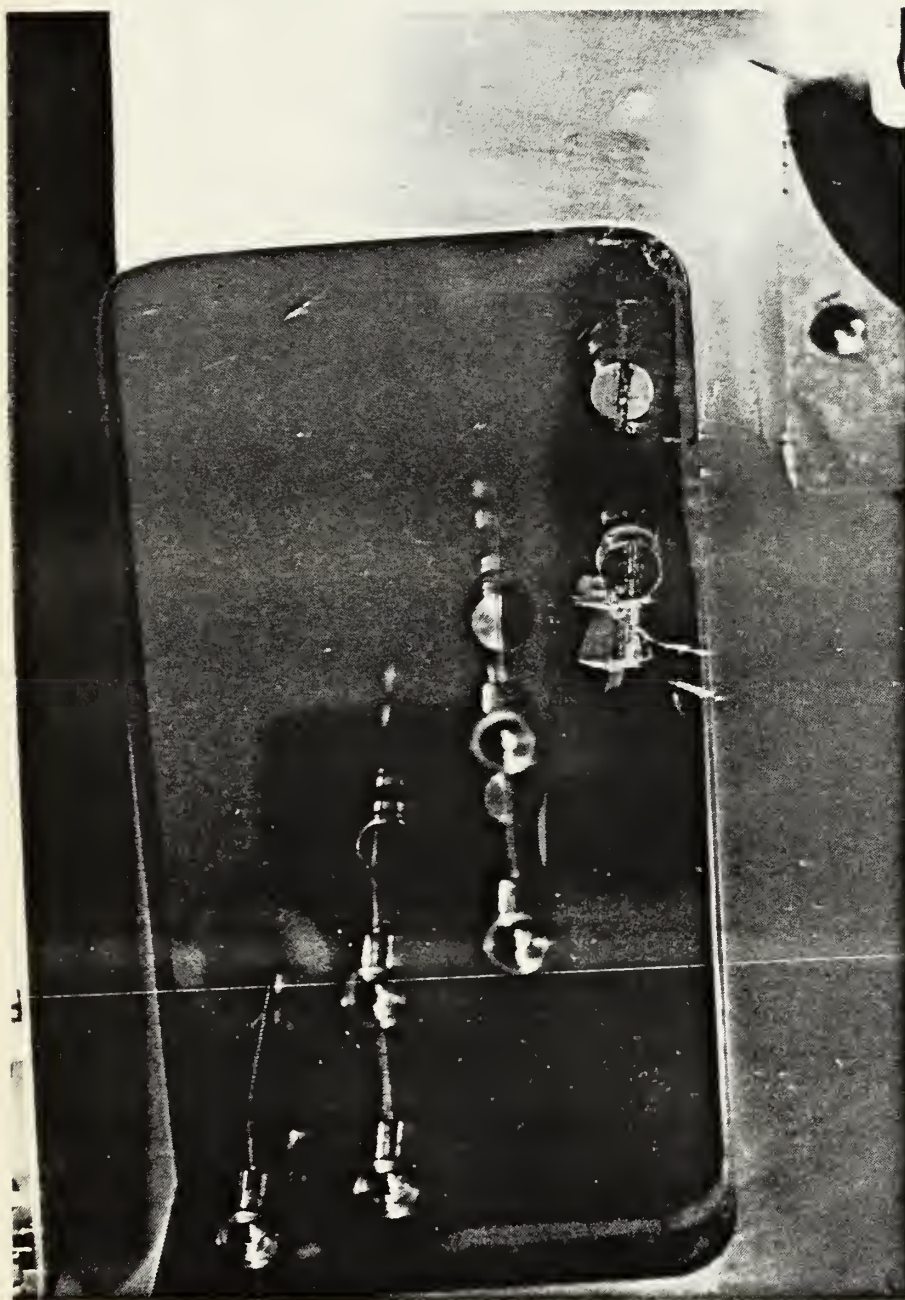
b. 2nd Blade from Upstream

Figure 16. (CONTINUED)



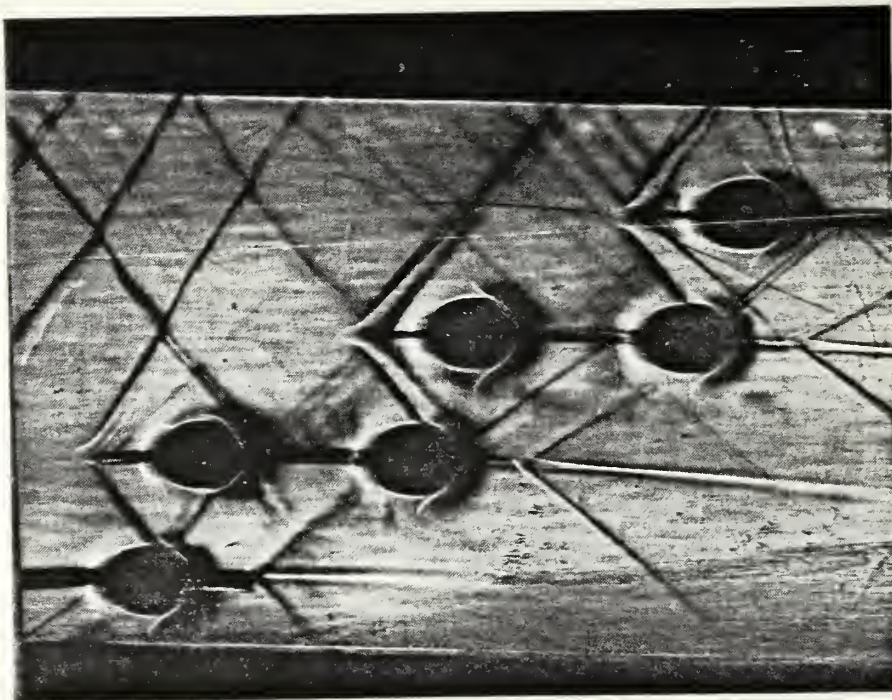
a. Left Side View

Figure 17. Test Section Following Failure of 1st Steel Blade

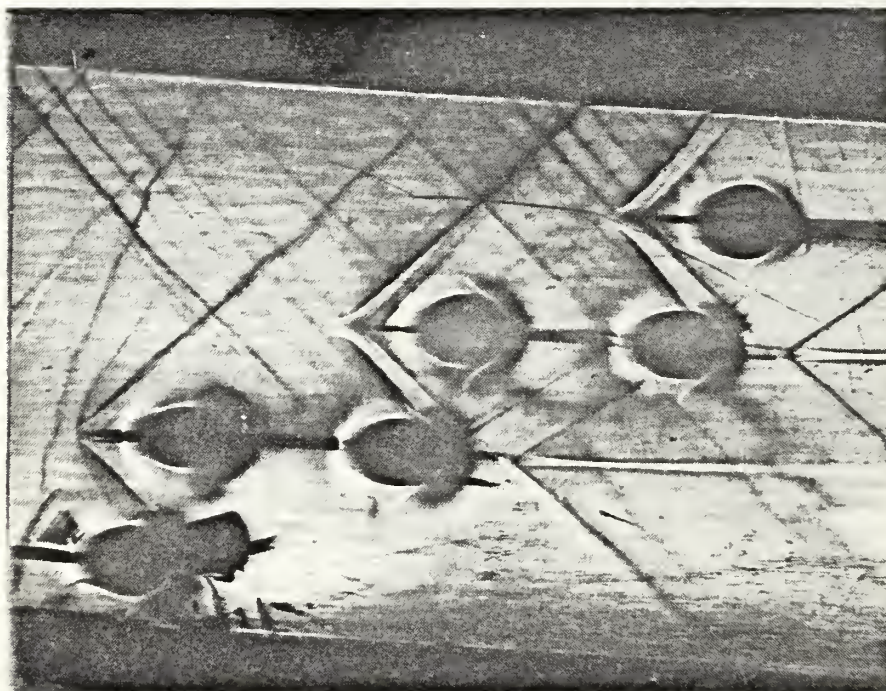


b. Right Side View

Figure 17. (CONTINUED)

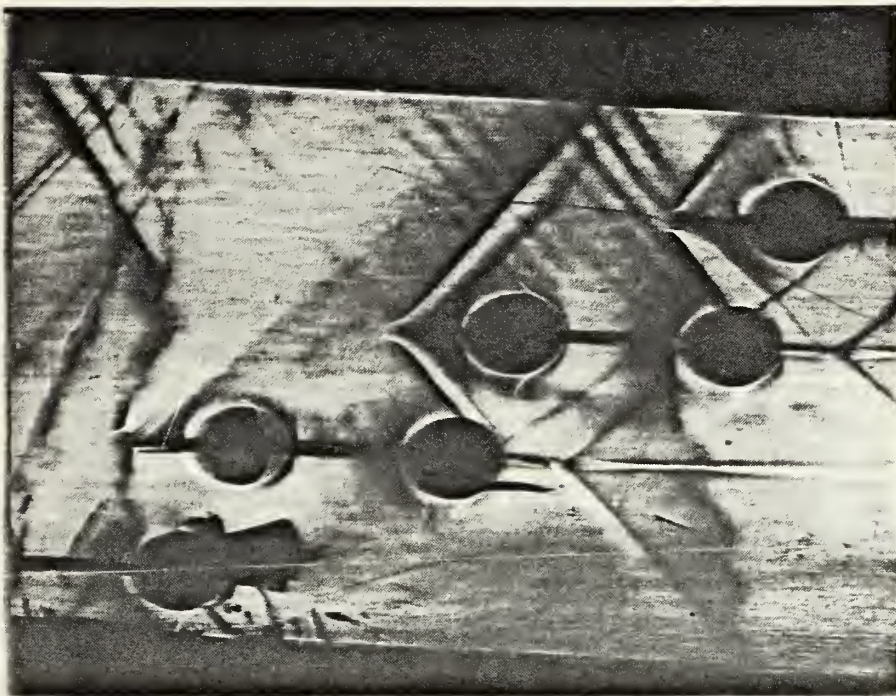


a. Prior to Blade Failure

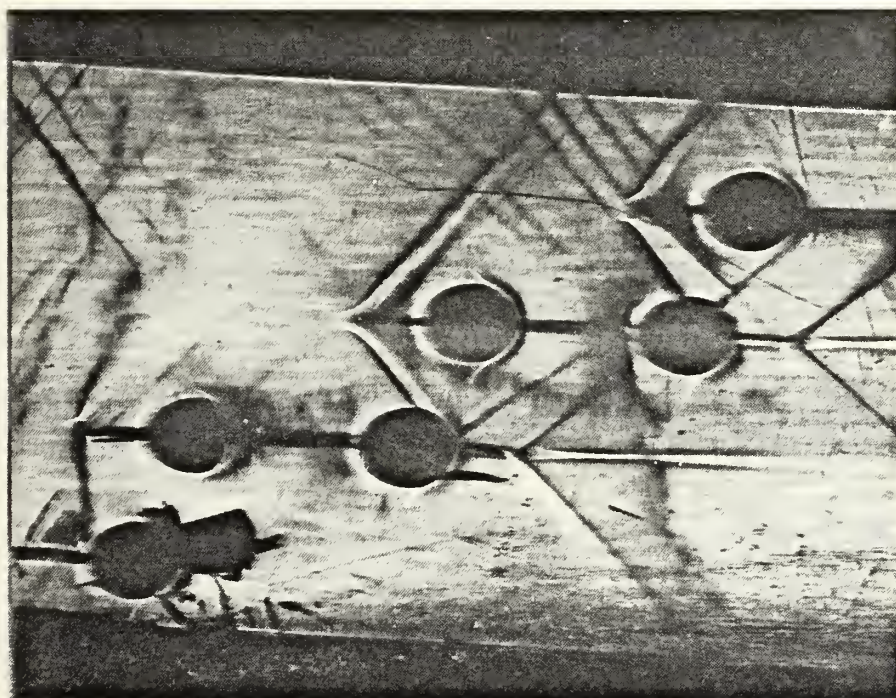


b. Flow Breakdown 1

Figure 18. Flow Characteristics During and Subsequent to Steel Blade Failure



c. Flow Breakdown 2



d. Flow Breakdown 3

Figure 18. (CONTINUED)

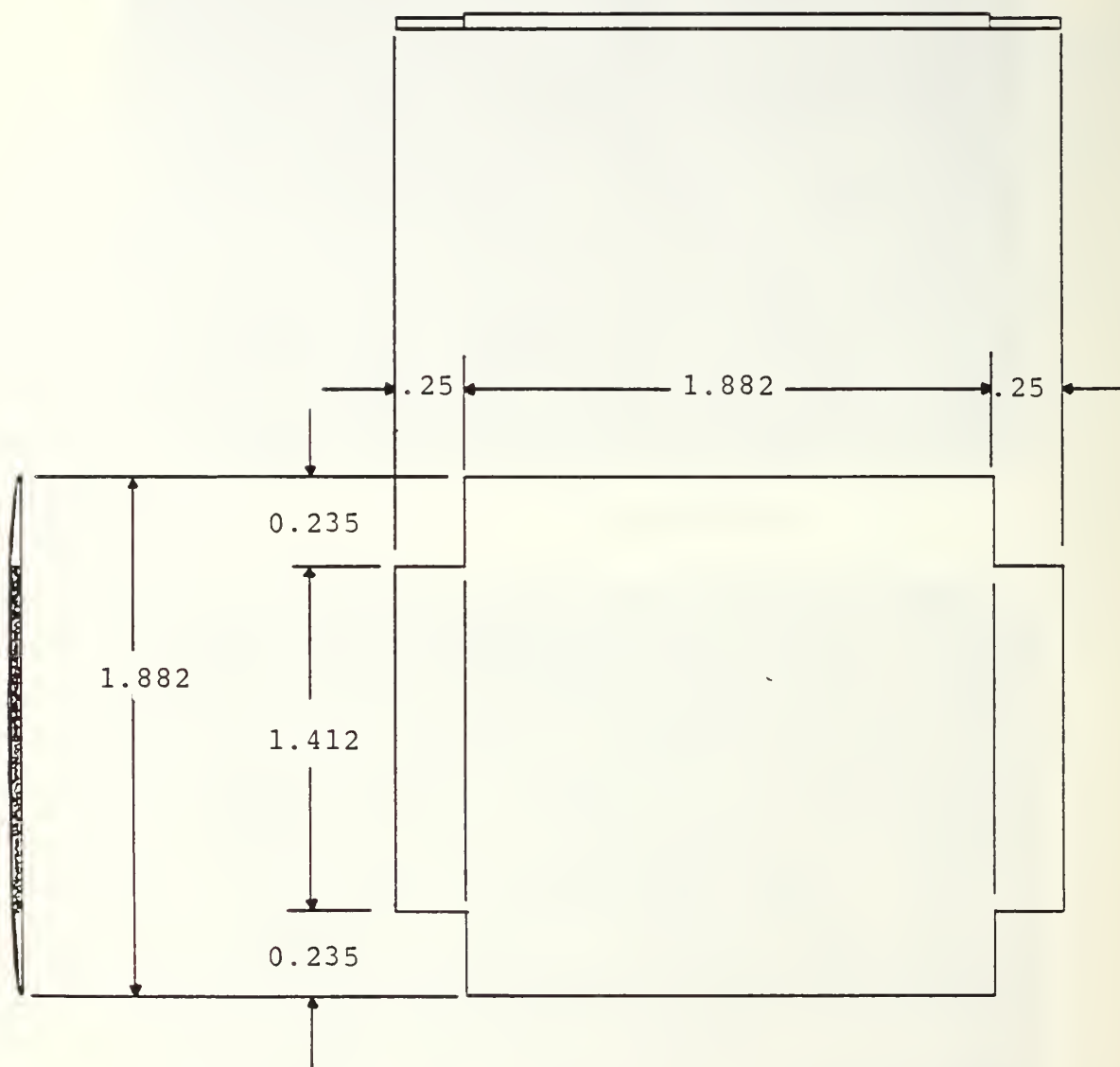


Figure 19. Redesigned Blade Mount

APPENDIX A
OPTICAL SYSTEM OPTIMIZATION

A1. BACKGROUND

Each application of Schlieren optics for flow visualization is different depending on the equipment available, the physical constraints of the wind tunnel environment and the desired observations. System sensitivity is increased by a factor which depends on the number of light beam passages through the test section [Ref. 7]. An even number of passes can be used to cancel distortion produced by refraction in the sidewalls. Simple systems lead to increased reliability and provide relative ease of alignment. A simple, single pass system was selected for the present application (Fig. 5).

A2. SYSTEM COMPONENTS

Characteristics and performance parameters for the optical system components are listed below:

1. 1000 watt continuous light mercury vapor source used for Schlieren photography and test section flow monitoring (Fig. A1).
2. 200-300 nanosecond spark light source used for shadowgraph photography (Figs. A2 & A3).
3. Parabolic front surface mirror with 97.5 inch focal length (mirror 1 in Fig. 5).
4. Parabolic front surface mirror with 48.0 inch focal length (mirror 2 in Fig. 5).
5. Front surface flat mirror used to select between light sources (Fig. A4).

6. Camera/viewing screen with shutter capable of manual operation or automatic exposure times down to 1/1000 of a second.
7. Spectra Physics 155 Helium-Neon laser with a 0.95 milliwatt output at a wavelength of 632.8 nanometers (for system alignment).

A3. SETUP

For Schlieren system operation the test section event must be in focus at the camera/viewing screen and the knife edge (Fig. A5) must be placed at the focal length of the mirror immediately upstream in the light path (mirror 2). Desired image size at the camera/viewing screen is related to object size and mirror focal length by the equation

$$1/o + 1/i = 1/f \quad (A1)$$

where o is the object distance, i is the image distance and f is the mirror focal length [Ref. 15]. An image magnification of 1.0 was selected for the present application based on test section and camera sizes.

Mirror focal lengths must be known and must be compatible with the design of the system. Unknown focal lengths were determined by taking an infinitely distant source (distance $\gg \gg$ focal length) and measuring the distance from the mirror to the minimum spot size of the reflected source.

The focal length of mirror 2 and the desired image magnification fix the mirror distance from the object (test section) and from the knife edge and camera/viewing screen. The light source must be placed at the focal length of

mirror 1 (Fig. 5). A flat mirror that could be moved in and out of the light paths was used to select between the continuous and spark light sources. There is no restriction on the distance from mirror 1 to the test section provided a parallel beam can be maintained. System sensitivity is a function of source intensity and the angles made by the light paths [Ref. 7]. Minimizing these angles helps to maximize sensitivity for a given system. Optimum component positioning subject to all these considerations determined the present optical system geometry.

A4. ALIGNMENT

Optical axis alignment is critical for minimizing distortion caused by refraction in a single pass system. Minimum refraction occurs when the axis is perpendicular to the test section sidewalls. Perpendicular alignment was obtained using a laser. A suitable low power laser with visible output was directed through the test section to mirror 1 (Fig. A6). A laser beam perpendicular to the test section sidewalls produced a single focused speckle pattern on entry and another on exit from each sidewall. Misalignment gave multiple reflections. The beam position was adjusted until it passed through the center of the test section and produced only 4 speckle patterns. Mirror 1 was then repositioned to center the laser spot and adjusted to reflect the spot to the center of the spark light source. This was an iterative process since correct focal length had to be

maintained. Once the spark source was aligned, the flat mirror was raised and repositioned to center the laser spot. The adjustment process was then repeated to center the laser spot in the continuous light source slit.

Once the light paths upstream of the test section were aligned the laser was repositioned to fire through the test section toward mirror 2. The same process of movement and adjustment was used (with knife edge retracted) to center the spot in the viewing screen.

A5. VERIFICATION/ADJUSTMENT

When the iterative alignment procedure was completed, a verification procedure was followed. With the continuous light source operating, a target of concentric circles was used to ensure that the light beam was parallel from mirror 1 to the test section and from the test section to mirror 2. A converging or diverging beam would require another iteration through the alignment process. It was also necessary to ensure the image reached a minimum spot size in the plane of the knife edge (Fig. A5). Small adjustments of knife edge position could be made at the camera without requiring realignment.

Once alignment had been verified the knife edge was moved in to provide the desired system sensitivity for Schlieren observations.

A6. OPERATION

Flow field density gradient observations and Schlieren photographs were made with the continuous light source operating. Polaroid type 52 film with a camera shutter speed of 1/1000 second was used for photographs. The optical system was always in this configuration (flat mirror up and knife edge moved in) for tunnel start and the establishment of the desired test condition.

Using the spark light source for shadowgraphs required lowering of the flat mirror and moving the knife edge aside. With the lab darkened the camera shutter was opened just prior to manually triggering the spark. Following the flash the shutter was closed to minimize film exposure to background light. The spark gap was adjusted to operate at 6 kilovolts. Polaroid type 52 film was used and neutral density filters were not required to achieve the desired contrast.

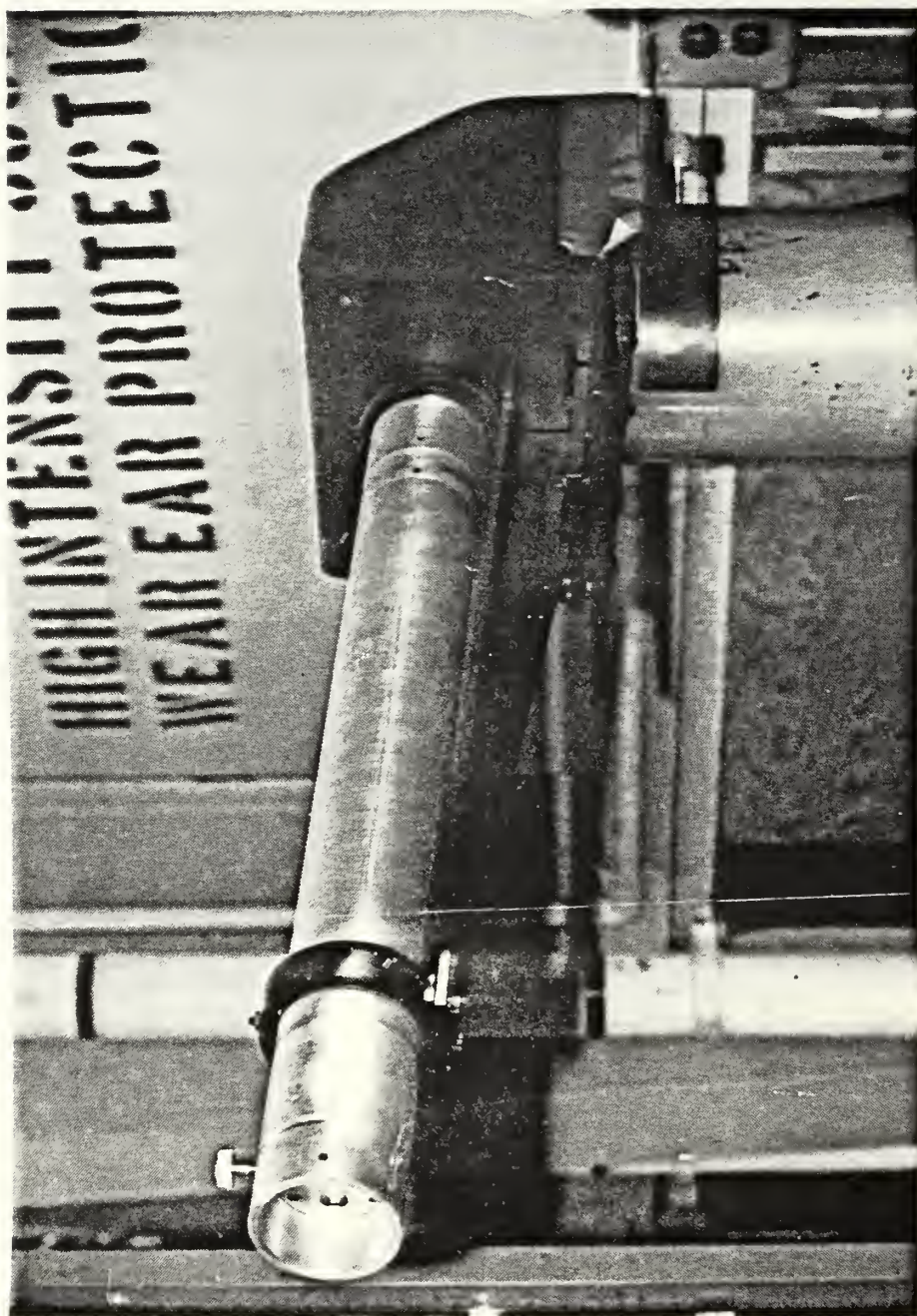


Figure A1. Continuous Light Schlieren Source

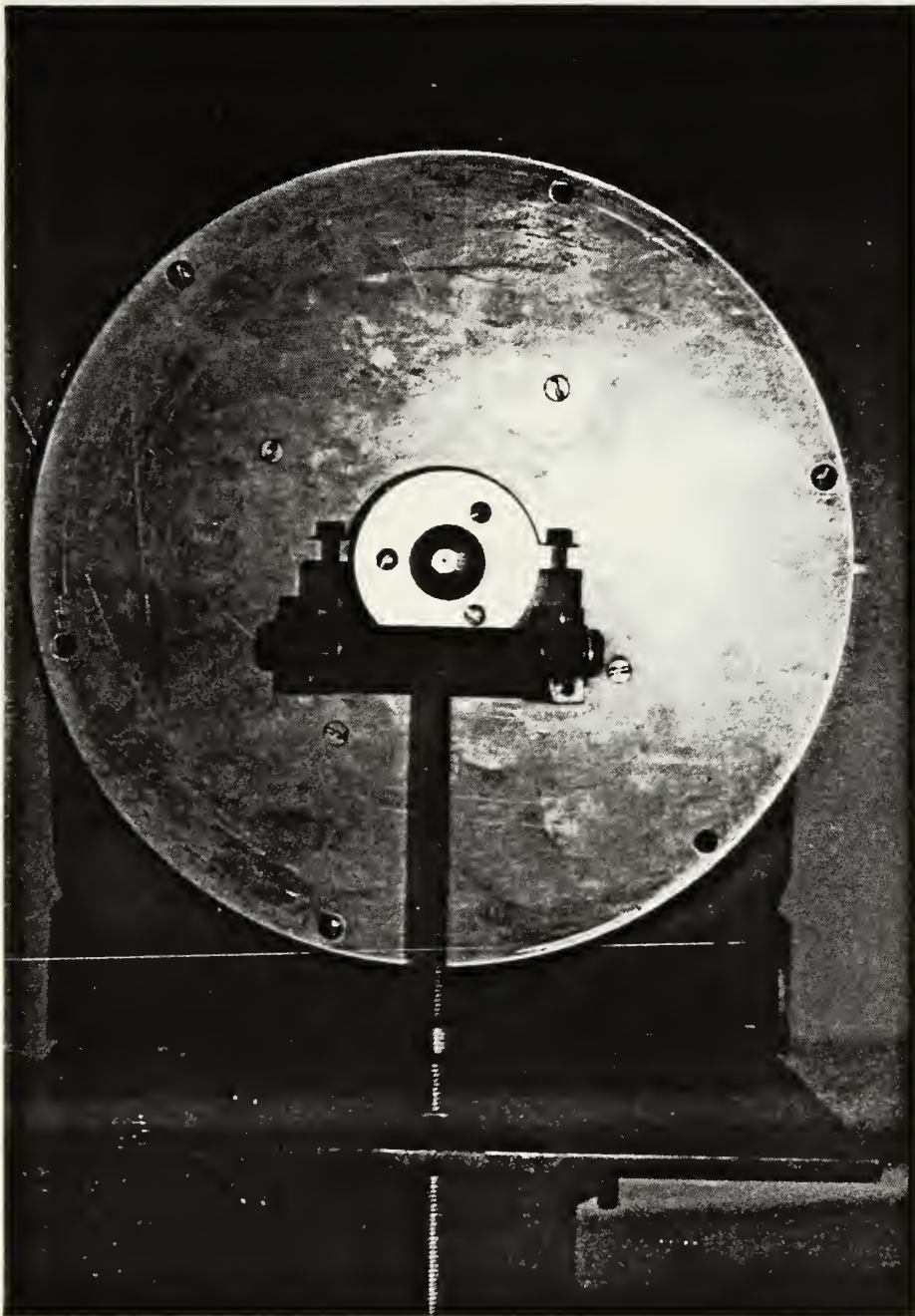


Figure A2. Spark Light Source

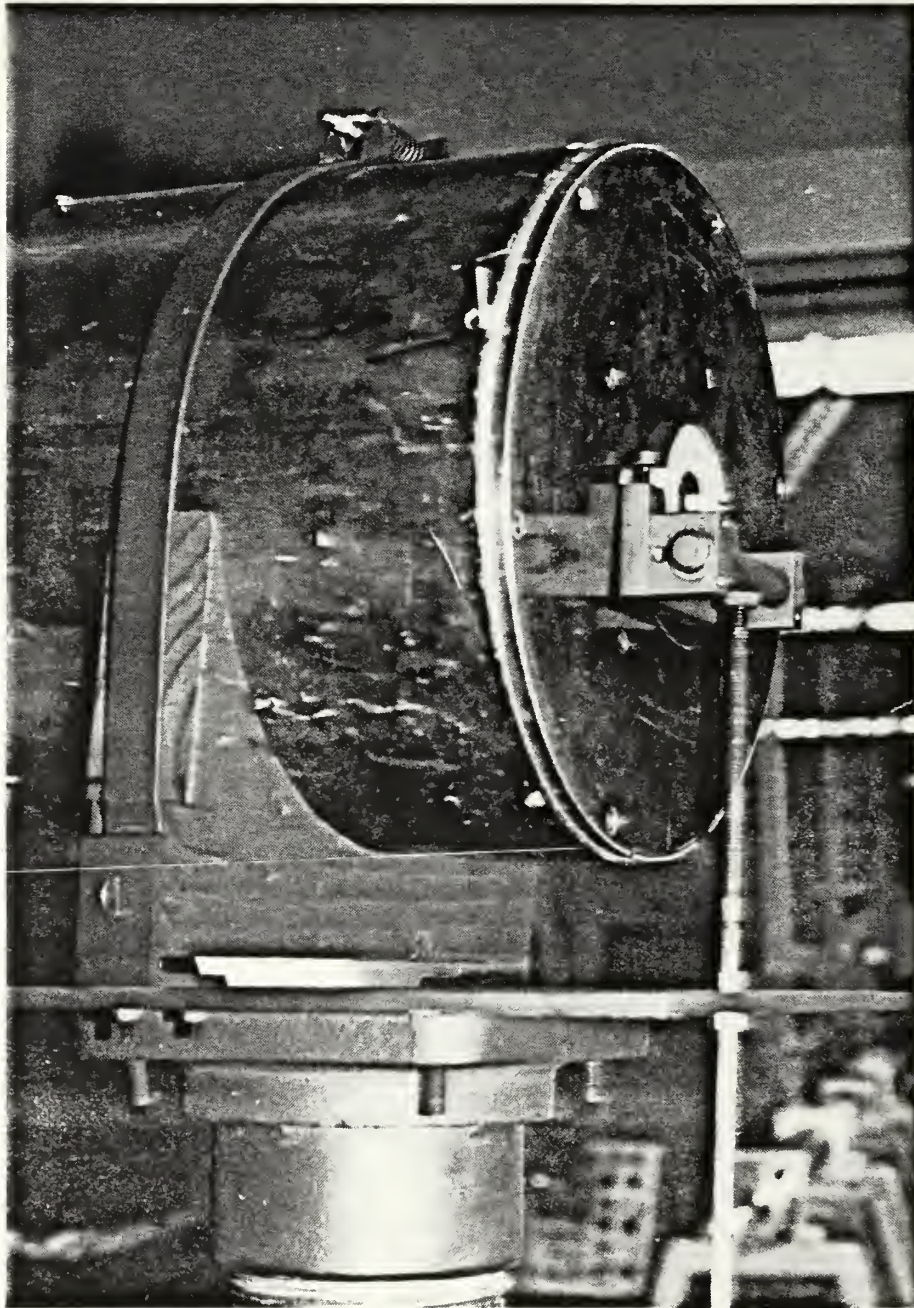


Figure A3. Spark Light Source Installation. (Adjustment Mechanism Provided One Degree of Freedom Motion for Axis Alignment.)

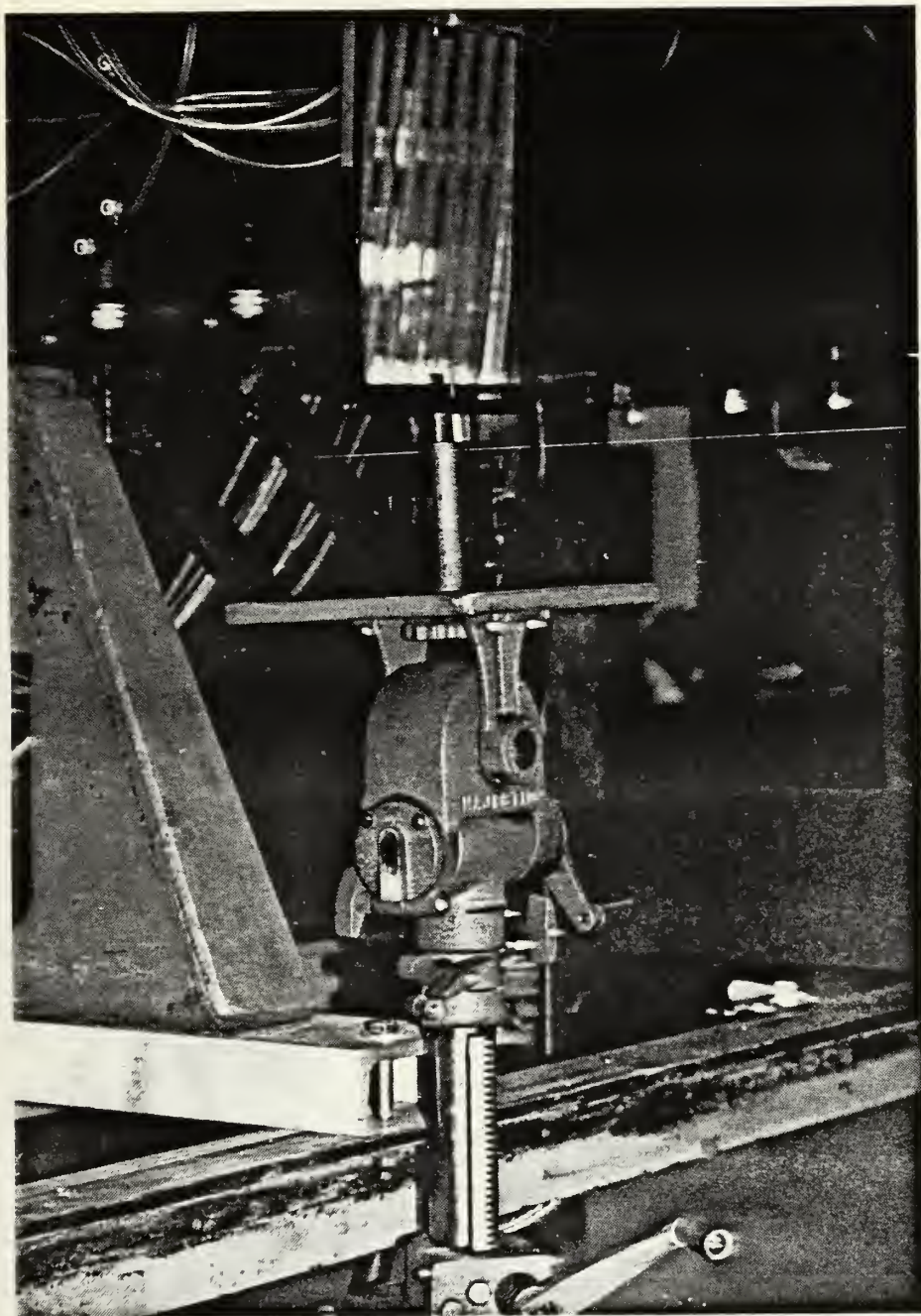


Figure A4. Light Source Selecting Mirror. (With Mirror Up, Test Section Is Illuminated With Continuous Light Source. With Mirror Down, Test Section Is Illuminated by the Spark Source.)

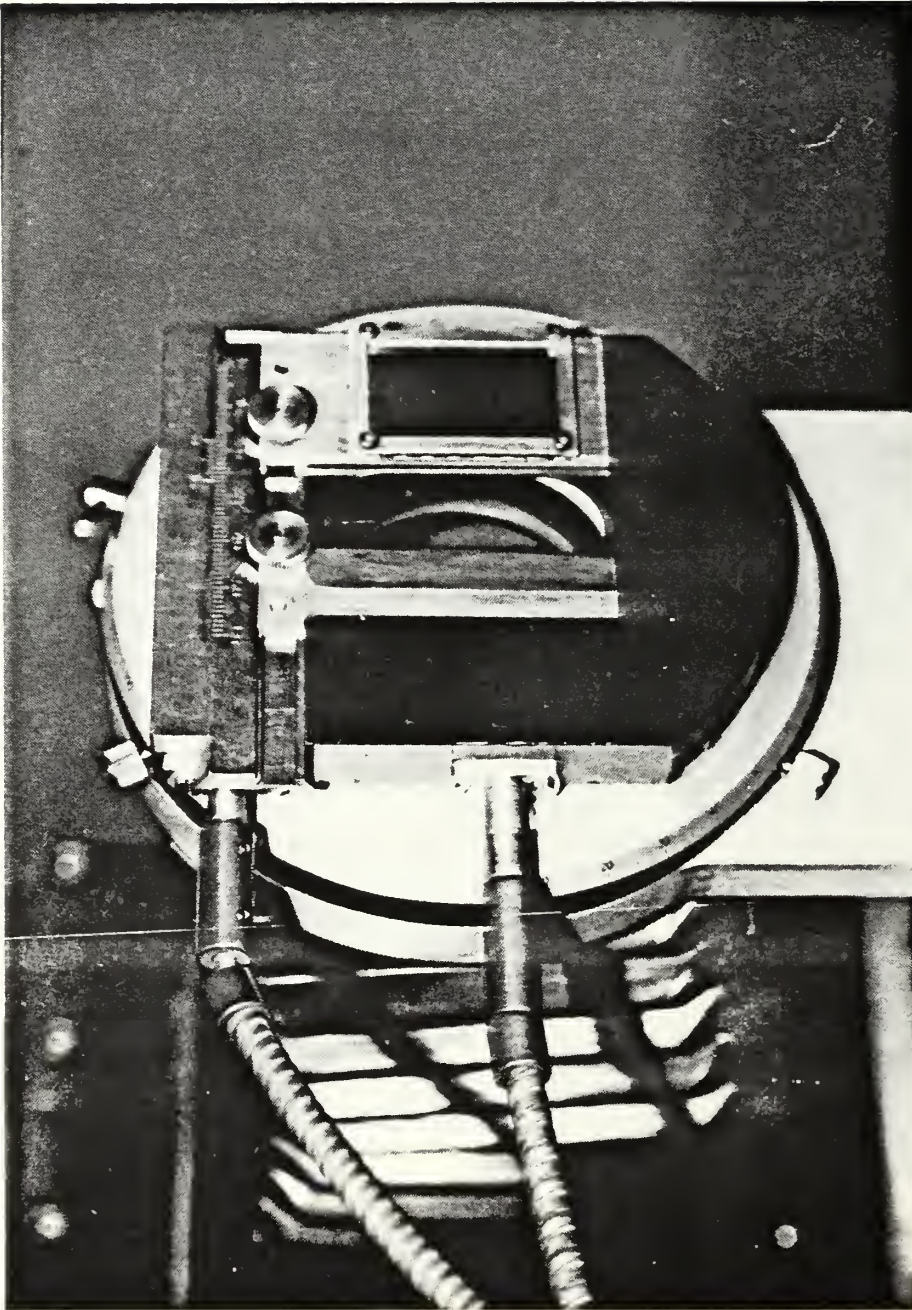


Figure A5. Schlieren Knife Edge

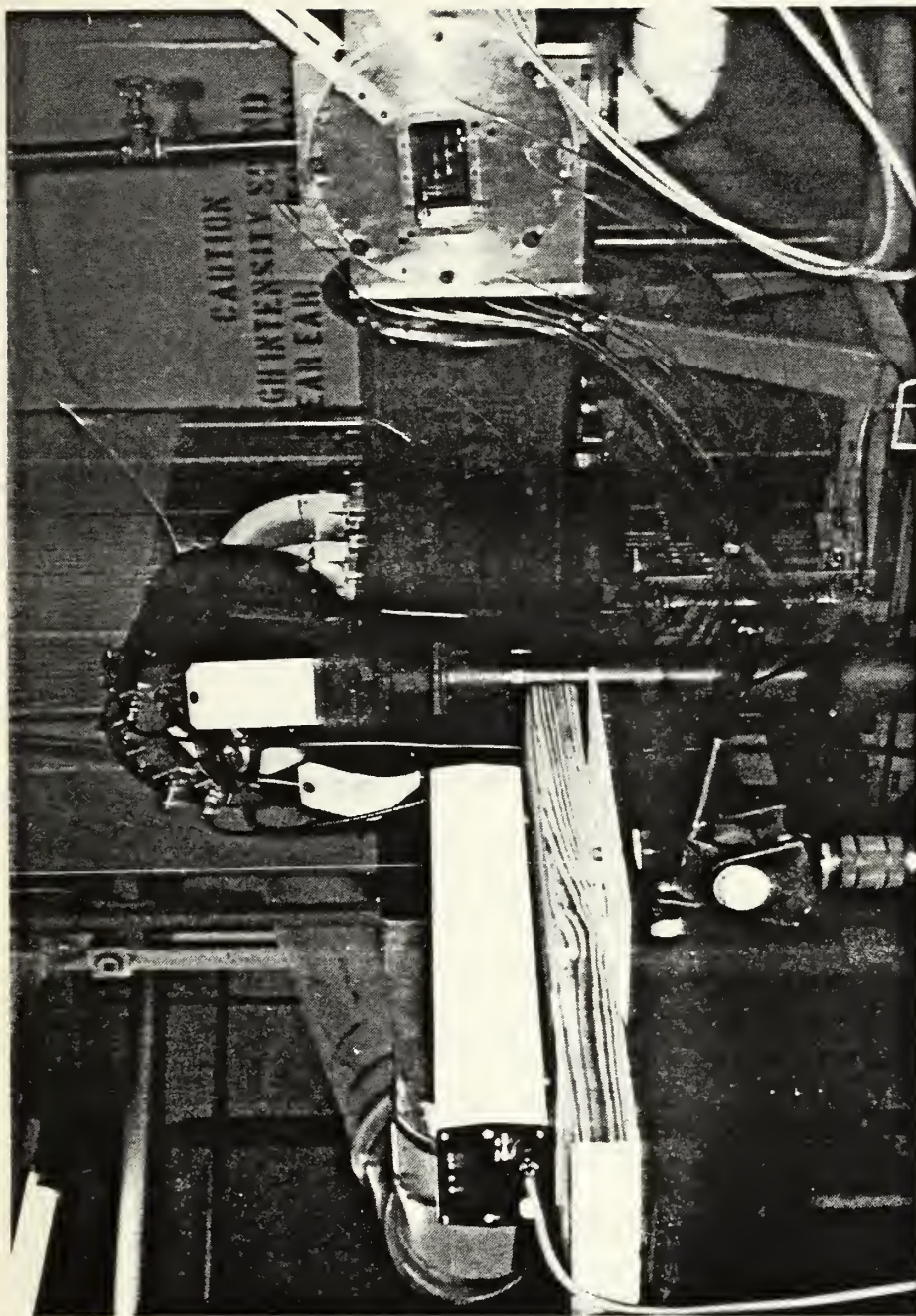


Figure A6. Laser Alignment. (Laser Fires Through the Test Section Sidewalls to Provide a Perpendicular Optical Axis for Alignment.)

APPENDIX B

BACK PRESSURE CONTROL

B1. BACKGROUND

Back pressure control in the cascade was necessary to produce a simulation of the flow conditions in a compressor blade row [Ref. 2]. The ramp-and-drum throttle valve assembly was designed in 1983 [Ref. 6] to meet this need. Operational requirements included quick, easy actuation, precise controllability and negligible blockage to the flow when not in use. The general arrangement of the assembly is presented in Figures 7 and 8. Figures B1 and B2 show the ramp control valve and ramp actuator respectively. The 3-spoke wheel for manually positioning the drum is shown in Figure B3.

B2. OPERATION

On the first test run with the throttle assembly installed the ramp was sucked up prematurely by supersonic flow through the valve. On subsequent tests the ramp was held down by supplying 100 PSIA shop air to the down side of the ramp actuator (Fig. B2). Once the test section had been started and an upstream stagnation pressure of 50 PSIA was established, the ramp was actuated by overdriving the shop air with high pressure nitrogen. Ramp position during

testing was either full up or full down since there was no purpose or mechanism for selecting intermediate positions.

With the ramp up, back pressure was varied by movement of the eccentric drum (Fig. 7). Control positions (Fig. B3) corresponding to drum flush with the passage sidewall (0% drum) and maximum extension (100% drum) were measured. Total travel was measured to be 0.488 inches which corresponded to approximately 5.6 square inches of available area change. Drum position settings corresponding to flush and maximum extension were 180° apart (Fig. B3). The flow was always started with a setting of 0% drum.

Friction provided by a rubber lining in the drum housing proved to be effective in setting and maintaining a desired drum position. Excessive friction rendered the drum virtually immovable while insufficient friction allowed the drum to rotate and change its setting. Friction was adjusted using the retaining hardware.

A small, unpredictable amount of leakage past the throttle valve components was inevitable. This necessitated a trial and error approach to adjusting the ramp-to-drum gap for a desired backpressure, but this presented no difficulty.

B3. ADJUSTMENT

The gap established by ramp actuation alone set the lower limit of the throttling range. Drum travel provided a range of throttling capability above this lower limit. By increasing the ramp extension the throttling range was

shifted to higher back pressures. Ramp extension was increased by lengthening the ramp actuator. Minimum gaps were measured before and after each adjustment by selecting 100% drum and slowly raising the ramp. A plug of clay on the ramp was deformed by contact with the drum. Measurement of the minimum clay thickness provided a measure of the minimum gap.

In each adjustment the actuator was lengthened by only a percentage of the previous gap (50%) to insure unstarting of the test section with 0% drum selected would be avoided.

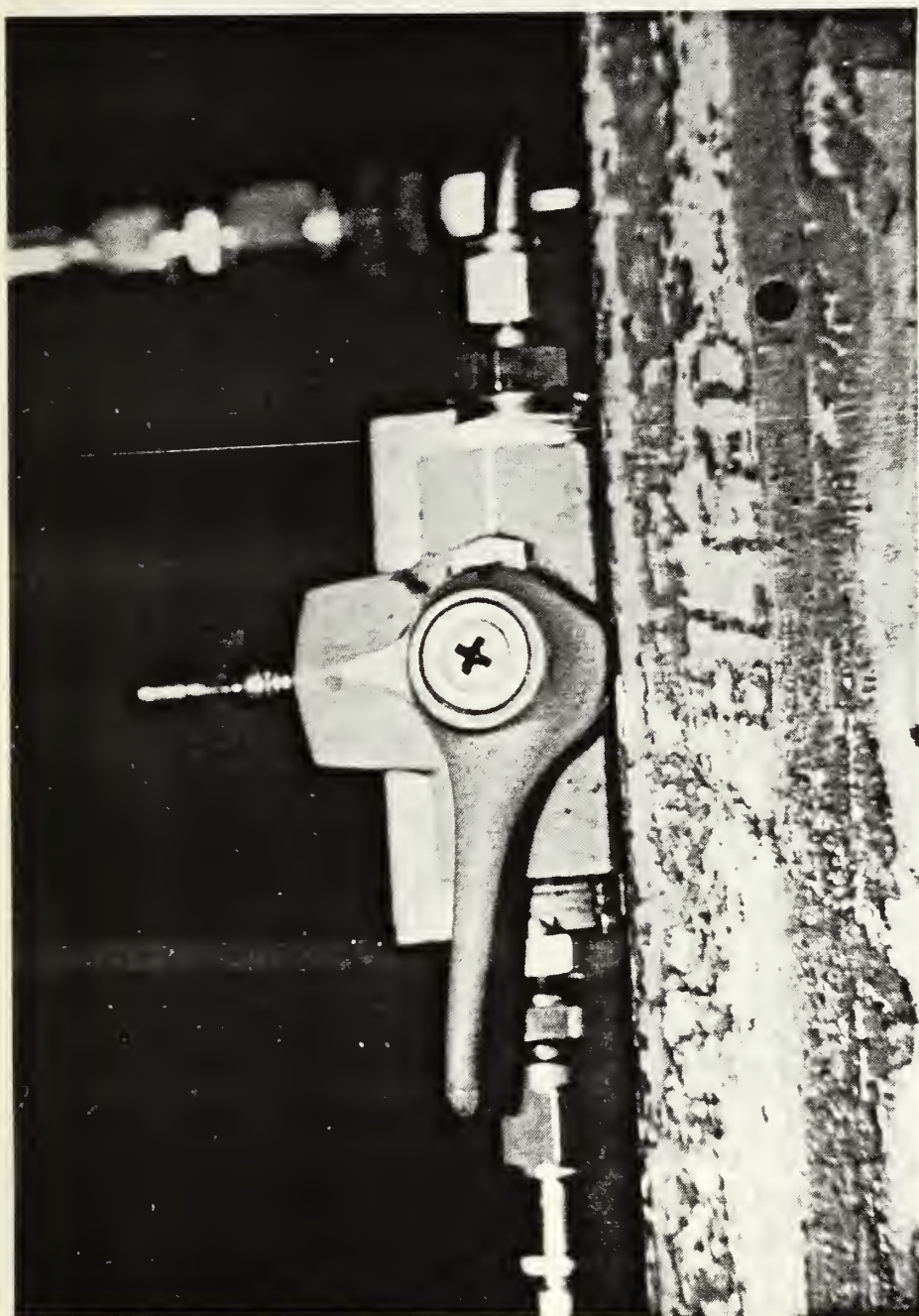


Figure B1. Ramp Control Valve

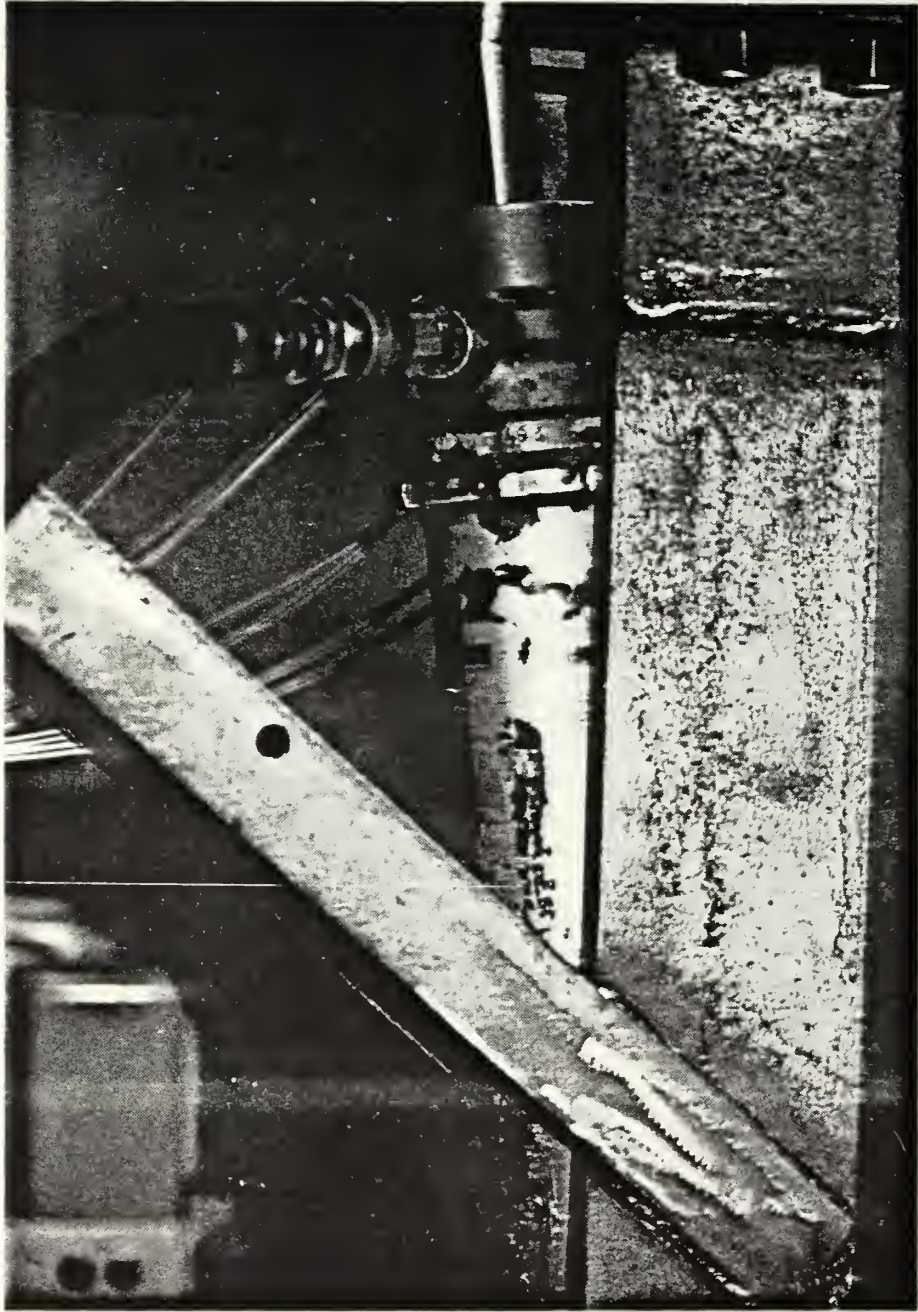


Figure B2. Ramp Actuator

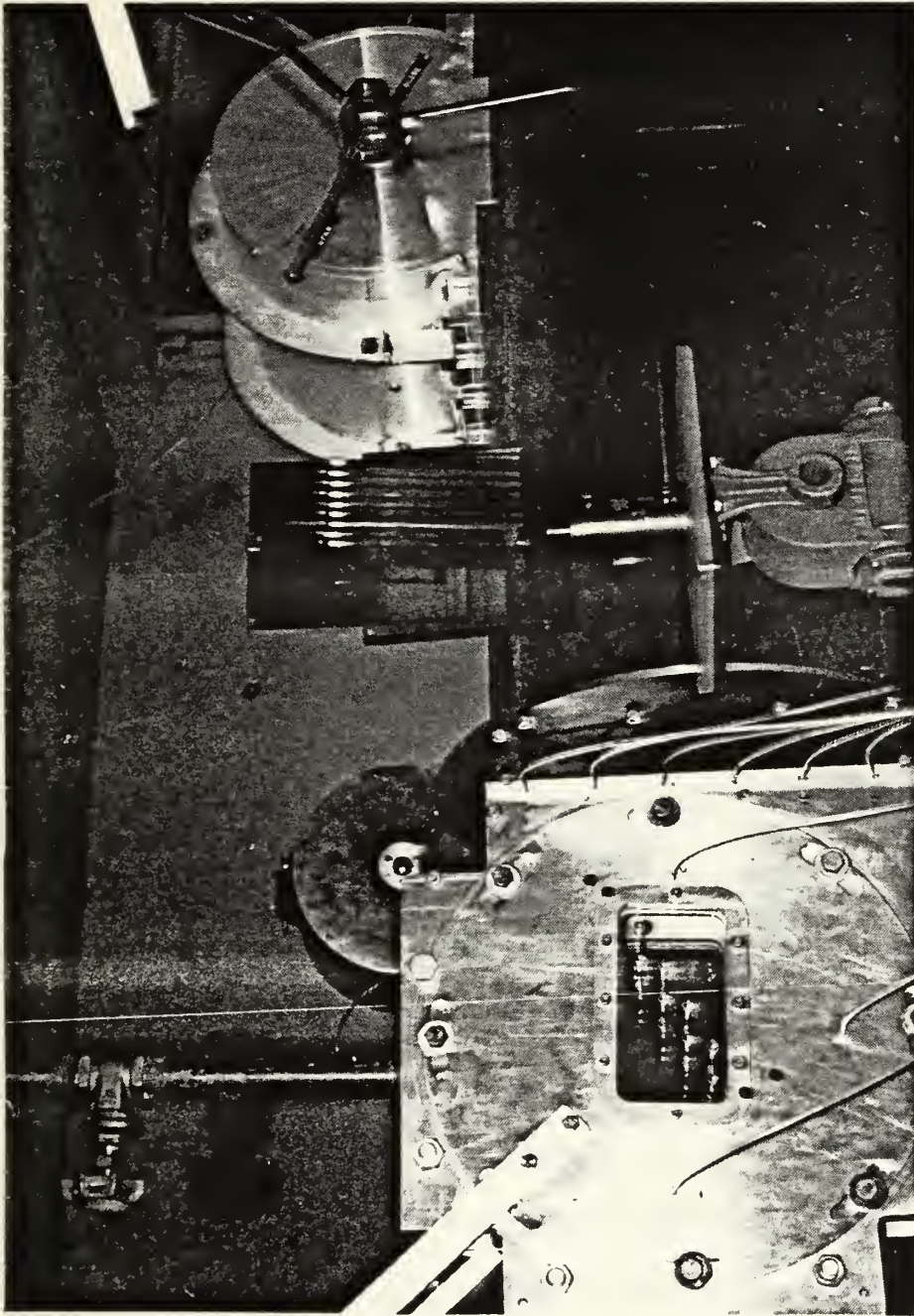


Figure B3. Drum of Back Pressure Control Valve Showing Manual Actuator

APPENDIX C
FLOW OSCILLATION MEASUREMENT

C1. BACKGROUND

Numerous studies have documented unsteady flow phenomena in transonic compressors and cascades (e.g., Refs. 16 and 17). Trailing edge vortex shedding and shock system oscillation are of particular interest. Vortex shedding has been postulated as a mechanism for driving shock system oscillation [Refs. 16,17]. Movement of the shock system about an average position results in shock Mach number variation with a corresponding variation in shock strength. The nonlinear increase in entropy across a shock with increasing Mach number results in a net increase in losses due to shock oscillation [Refs. 16,17,18].

Heinemann et al., developed a nonintrusive electro-optical method of measuring vortex shedding frequencies in a transonic turbine cascade [Refs. 19,20,21]. These methods have been adapted and modified for use in measuring shock oscillation frequency as well as vortex shedding in the NPS/TPL transonic compressor cascade (Fig. C1). Because of blade failures, the measurements were not carried out. However, the design of the measurement system and the intended procedures are described herein.

C2. SYSTEM COMPONENTS

Characteristics and specifications for the measurement system components are listed in the following paragraphs.

1. Sensor (Fig. C2): The sensor assembly contains two key subcomponents, an HUV-1100BQ photodiode and a 0.003 inch pinhole. The HUV-1100BQ is a silicon photovoltaic detector with high sensitivity in the ultra violet range and very high frequency response (up to 5 megahertz). Operating data and performance specifications for the HUV-1100BQ are listed in Table C1. The photodetector is mounted to the back of the laser drilled pin hole (Figs. C3 and C4). Discussions with Heinemann indicated the pin hole must be small in relation to the event of interest. 0.003 inches was estimated to be nearly an order of magnitude smaller than the shock width which was the limiting dimension (shock width taken from steady flow Schlieren photographs).
2. Support stand: A vibration damped support stand was constructed to hold the sensor. Mounted atop the support was a positioning device capable of accurate movement in vertical and horizontal directions.
3. Tektronics model 551 oscilloscope: Used for monitoring sensor output.
4. 1000 watt continuous light Schlieren source: Illumination of the test section is provided by the continuous light Schlieren source. The majority of output energy from the mercury vapor lamp is concentrated in the ultra violet region of the spectrum and dictated the selection of a sensor with high sensitivity in this range.

C3. MEASUREMENT PROCEDURES

The sensor must be prepositioned prior to tunnel starting. This position will be determined from Schlieren photographs and shadowgraphs (spark gap shadowgraphs are required to resolve vortex shedding from photographs) taken at the desired run condition. After locating the desired event with reference to the test section the sensor can be positioned

by a process of laser alignment. The laser would be directed through the test section at the point corresponding to the event of interest to the sensor.

Small adjustments of position to optimize the sensor output will be required with the tunnel running while monitoring the oscilloscope. Oscilloscope traces can be recorded photographically to provide the desired frequency data.

Once frequency measurements are completed shock wave oscillation amplitude can be estimated by traversing the sensor in the direction of shock oscillation. By noting the distance traversed from the onset of oscillation to the point where oscillations disappear the amplitude of the oscillation can in principal be deduced.

TABLE C.1

HUV-1100BQ OPERATING DATA
AND PERFORMANCE SPECIFICATIONS

Active Area	5.1 mm ²
Spectral Range	185-1150 nm
Frequency Range	DC-5 MHz
Slew Rate	12 Volts/ μ sec
Supply Voltage	± 5 to ± 18 Volts
Supply Current	50 milliamps at ± 15 Volts
Power Consumption	150 milliwatts at ± 15 Volts
Operating Temperature	0 to 70°C

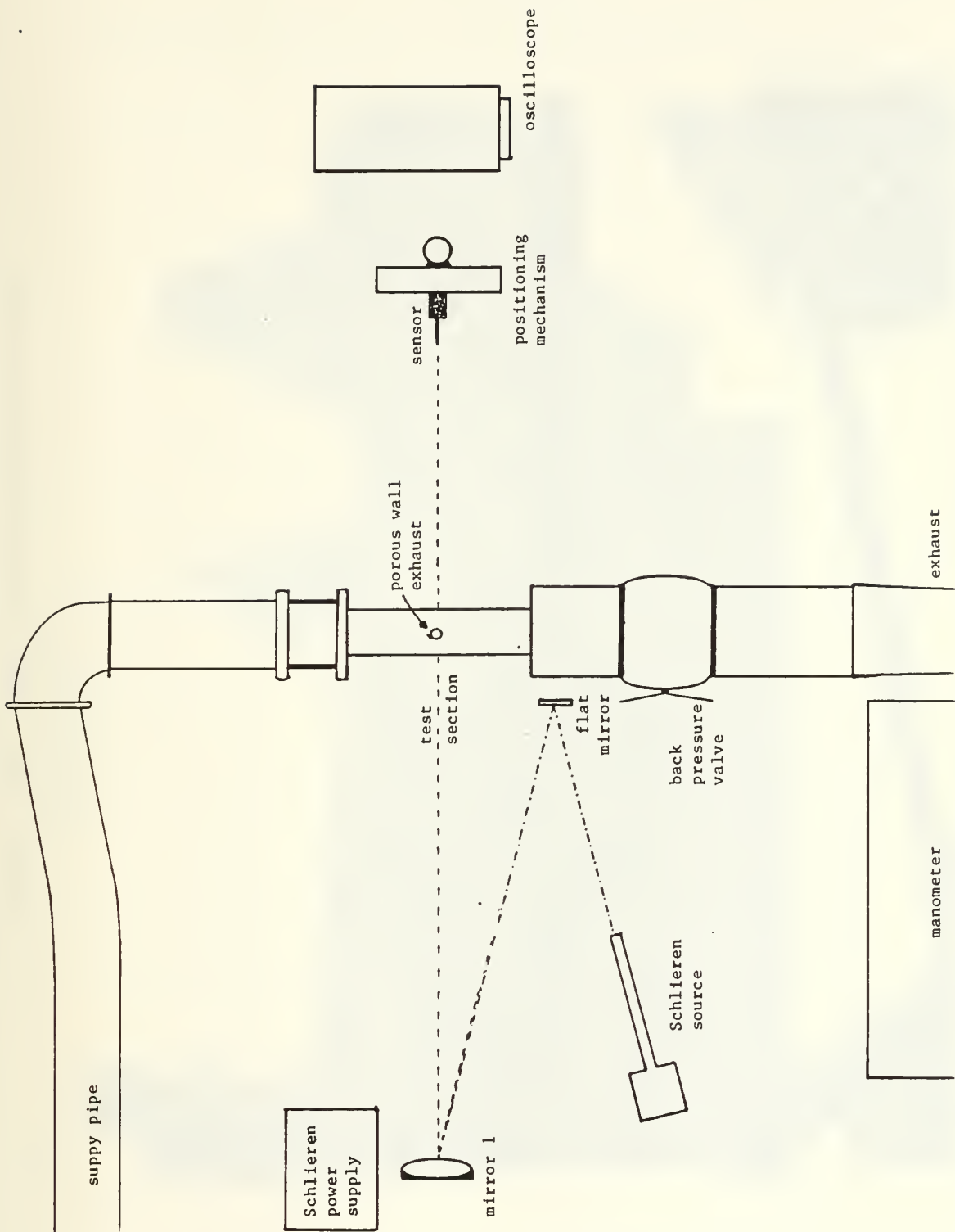


Figure C1. Oscillation Measurement Apparatus Layout

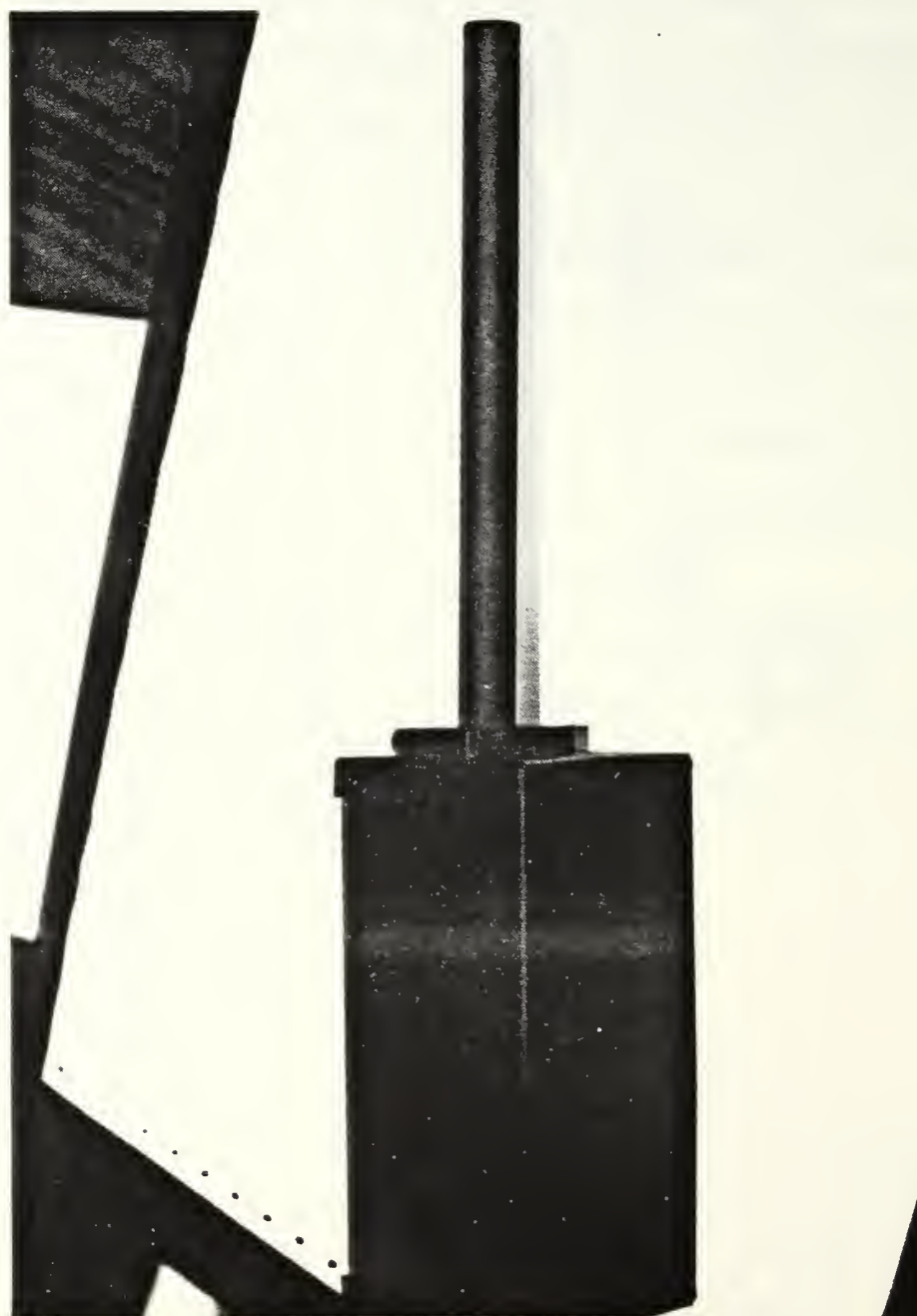


Figure C2. Oscillation Sensor Housing

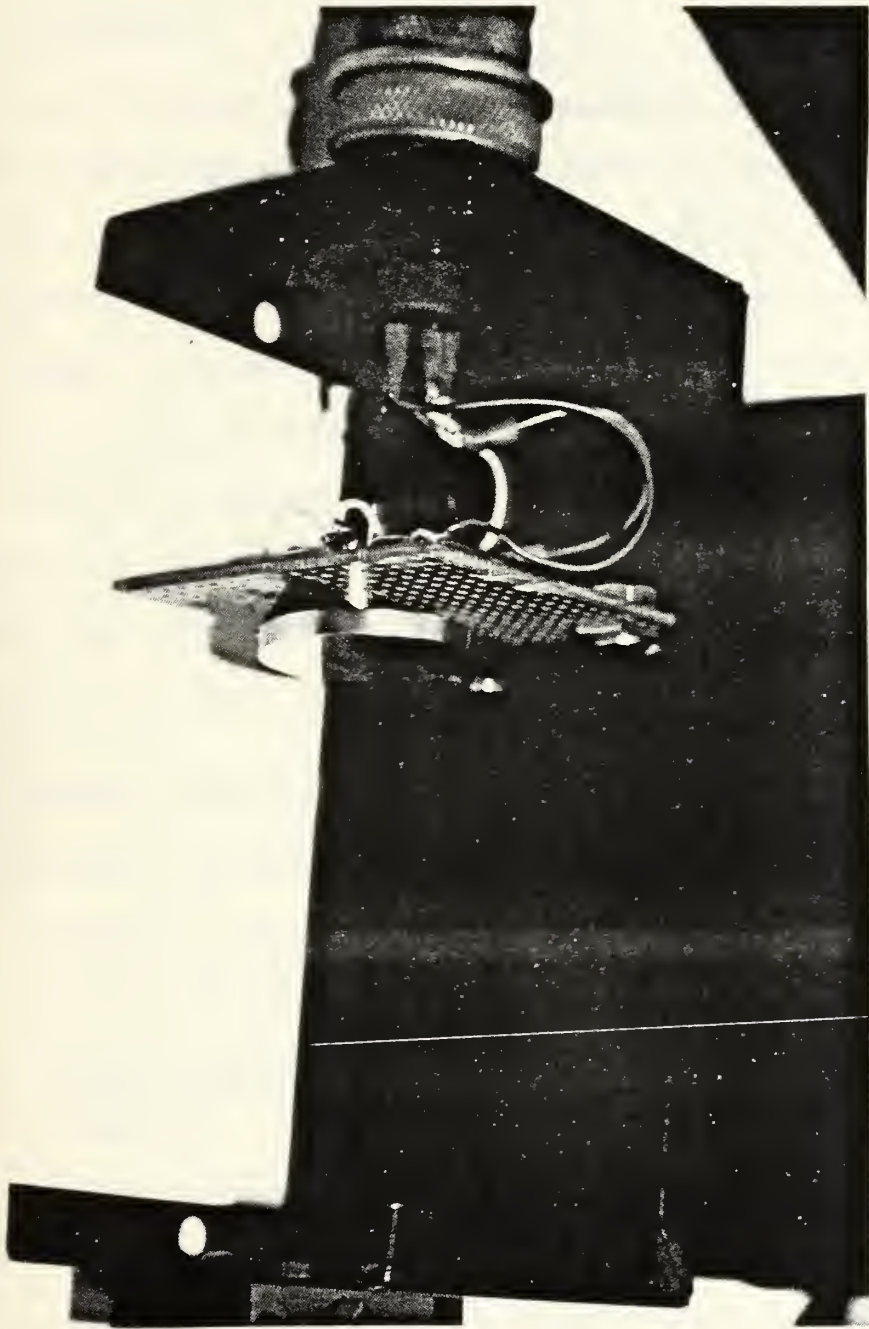


Figure C3. Pinhole and Photodiode Installation

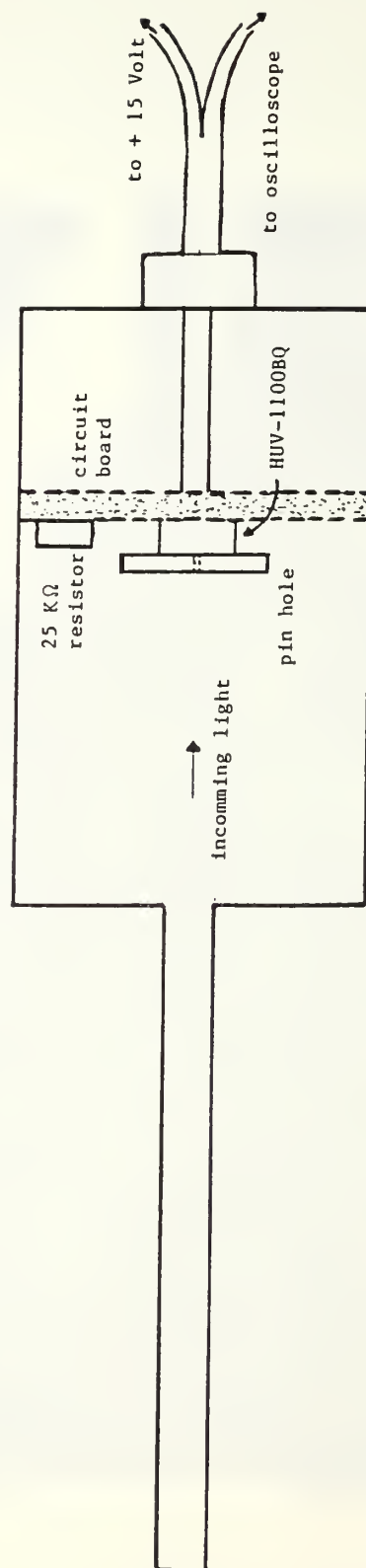


Figure C4. Oscillation Sensor Cutaway

APPENDIX D

TRANSONIC COMPRESSOR CASCADE OPERATING PROCEDURES

D1. BACKGROUND

The following procedural checklists were developed from previous experience [Ref. 2] and lessons learned during early testing. The checklist format was selected to ensure that a reproducible pattern with no omissions was followed in every test. Responsibility for the various steps was distributed among those preparing for and executing the test. Pretest briefings, where the test objectives were defined and individual responsibilities assigned, were conducted prior to each run. A minimum of three people were required to conduct a test.

D2. PRESTART CHECKLIST

- (1) start Joy-Sullivan compressor
- (2) pump air storage tank to approximately 275 PSIA
- (3) remove tunnel exhaust cover
- (4) turn on continuous light Schlieren source power supply filaments (minimum warmup of 15 minutes required)
- (5) check Heise gauge reads atmospheric pressure
- (6) check data camera for film and proper flash operation
- (7) check Polaroid film for Schlieren/shadowgraph pictures
- (8) check all tunnel attaching hardware for security

- (9) check porous wall exhaust control valve for desired position
- (10) turn on spark source power supply and set rheostat to 70 (corresponding to 6 kilovolt operating voltage)
- (11) position flat mirror up for continuous light system monitoring during test start-up and adjustments
- (12) turn on manometer light
- (13) turn on shop air to ramp actuator
- (14) turn on continuous light schlieren source
- (15) perform ramp operational check
- (16) secure Joy-Sullivan compressor (after tank has been pumped up)
- (17) warn people in the vicinity of noise hazard.

D3. START/RUN CHECKLIST

- (1) vent ramp control valve and check valve closed and ramp full down
- (2) open main supply valve
- (3) open supply control valve and bring supply pressure rapidly to 50 PSIA
- (4) observe test section starting on Schlieren viewing screen and/or manometer
- (5) actuate ramp with high pressure nitrogen
- (6) select desired back pressure with eccentric drum
- (7) acquire desired data
- (8) record supply pressure from Heise gauge
- (9) close supply control valve when test is completed or when remaining air supply is insufficient to maintain 50 PSIA.

APPENDIX E
ANALYSIS OF EXPERIMENTAL DATA

E1. TEST SECTION AND POROUS WALL MASS FLOW

1. Test Section Flow

The continuity equation for steady, one-dimensional flow of a perfect gas [Ref. 22] can be expressed as

$$\dot{m} = pAM\sqrt{kg_c/RT} \quad (E-1)$$

Stagnation temperature and pressure under similar conditions are given by

$$T_t = T \left[1 + \frac{(k-1)}{2} M^2 \right] \quad (E-2)$$

and

$$P_t = P \left[1 + \frac{(k-1)}{2} M^2 \right]^{k/k-1} \quad (E-3)$$

At the nozzle throat the area is 6.27 in² [Ref. 1] and the Mach number is 1.0 assuming choked flow. For isentropic flow upstream of the throat and stagnation temperature constant at 518.7°R, application of equations of E1, E2 and E3 yields a mass flow of 7.33 lbm/sec.

2. Porous Wall Flow

In the outlet pipe from the porous wall, P was taken as atmospheric pressure and T_t again as constant at 518.7°R. Duct area was computed to be 0.785 in². Total pressure in the center at the duct exhaust was measured by a Kiel probe. Equations E1, E2 and E3 were applied without correcting for viscous blockage to obtain an upper estimate of the mass flow through the porous wall. This mass flow varied for different test runs depending on test section back pressure and bleed rate control value setting but was generally of the order of 2-3% of test section mass flow.

E2. BLADE PASSAGE PRESSURE AND MACH NUMBER DISTRIBUTION

The model used in blade passage pressure and Mach number calculations is shown in Figure E1. The passage was divided into upper and lower halves and calculations were carried out along the blade surfaces (pressure surface for the upper half passage and suction surface for the lower half passage). Shock angles were taken from 4 schlieren photographs and combined with deduced surface conditions to solve for the Mach number upstream of the shocks using [Ref. 22]:

$$\tan \delta = 2 \cot \theta \left[\frac{M^2 \sin^2 \theta - 1}{M^2 (k + \cos 2\theta) + 2} \right] \quad (E-4)$$

The averaged results of these calculations are listed in Tables E.1 and E.2. Fluid property changes across the shocks were computed using the tables of Reference 22.

1. Suction-side Calculations

The suction surface was divided into four equal segments. Prandtl-Meyer expansions were calculated at the discrete nodes separating these segments. Flow between nodes was taken as being unchanged. Equal expansions were taken at each node and flow characteristics along the suction surface were computed using the tables of Reference 22. Oblique shock impingement (Fig. E1) was estimated to occur midway between the third and fourth nodes. Half of the last expansion was calculated to occur prior to the shock and half after. Knowing θ (measured) and the upstream Mach number, δ was calculated using Equation E4. For flow parallel with the blade surface both upstream and downstream of the shock, equal streamline deflection must take place through the incident and reflected shocks. The details of shock wave-boundary layer interaction [Refs. 10,23] were not considered. Local separation at the interaction was estimated to be small due to the presence of a turbulent boundary layer and the curved nature of the suction surface in the vicinity of the shock boundary layer interaction [Ref. 23]. Results of these calculations are listed in Table E.3.

2. Pressure-side Calculations

Flow property variations along the upper half of the passage were calculated in similar fashion. Suction surface

expansions impinging on the pressure surface were not accounted for. Results of the calculations are listed in Table E.4.

3. Blade Row Exit Conditions

Exit flow from both upper and lower blade surface calculations was required to be parallel and to meet the downstream pressure boundary condition. Downstream pressure measurements were averaged and used to fix the conditions downstream of the shocks at the blade trailing edges. Results of these calculations are listed in Table E.5.

E3. BLADE ROW MASS FLOW

Mass flow through each blade passage was estimated by using the flow characteristics computed on the pressure surface over the upper half and flow characteristics computed on the suction surface over the lower half of the passage at the point of minimum passage area. Flow properties were treated as being constant from the blade surfaces to the center of the passage. Results of the calculations are listed in Table E.6. The computed total mass flow through all 5 blade passages was 5.45 lbm/sec. This represented 75% of the mass flow entering the test section. The porous wall bleed control was closed during the test runs for which these calculations were made giving zero net mass flow through the porous wall. This suggested that 25% of the flow passed out through the upper and lower boundary layer scoops. Since the scoops

represent only 13% of the test section area, at least 12% of the mass flow was not accounted for. This discrepancy gauges the inaccuracy involved in the approximations made in performing the flow field calculations.

E4. BLADE PRESSURE LOADING

Surface pressure distributions from Tables E.3 and E.4 were integrated along the blade chord to obtain blade loading. Pressure distributions over the blade surfaces are plotted in Figure E.2 as pressure coefficient. The normal pressure force per blade was calculated to be 6.8 lbf.

TABLE E.1

CHANGES ACROSS SHOCKS IMPINGING ON THE UPPER NOZZLE SURFACE

θ	M_1	P_2/P_1	P_{t2}/P_{t1}
43.8	1.49	1.074	0.99996
43.9	1.49	1.073	0.99996
43.1	1.51	1.075	0.99996
43.0	1.51	1.075	0.99996
45.1	1.46	1.080	0.99995

TABLE E.2

CHANGES ACROSS PASSAGE SHOCKS FROM BLADES 2, 3 AND 4

θ	M_1	P_2/P_1	P_{t2}/P_{t1}
50.3	1.40	1.180	0.9995
48.8	1.43	1.176	0.9996
49.3	1.42	1.174	0.9996

TABLE E.3

SUCTION SURFACE FLOW CHARACTERISTICS

<u>Station</u>	<u>M₁</u>	<u>P (PSIA)</u>	<u>P_t (PSIA)</u>
1	1.44	17.0	49.998
2	1.52	13.2	49.998
3	1.60	11.8	49.998
4	1.68	10.4	49.998
5	1.72	9.8	49.998
6	1.43	14.91	49.632
7	1.13	22.15	49.110

TABLE E.4

PRESSURE SURFACE FLOW CHARACTERISTICS

<u>Station</u>	<u>M₁</u>	<u>P (PSIA)</u>	<u>P_t (PSIA)</u>
2'	1.44	17.0	49.998
3'	1.52	13.2	49.998
4'	1.31	15.7	49.810

TABLE E.5

BLADE PASSAGE EXIT FLOW CHARACTERISTICS

<u>Station</u>	<u>θ</u>	<u>δ</u>	<u>M_e</u>	<u>$\Delta\beta$</u>
8	67.3	2.0	1.05	10.7
8'	68.6	5.0	1.01	8.3

TABLE E.6

BLADE PASSAGE MASS FLOW

<u>Passage half</u>	<u>Mass Flow (lbm/sec)</u>
upper	0.55
lower	0.53
total/passage	1.1

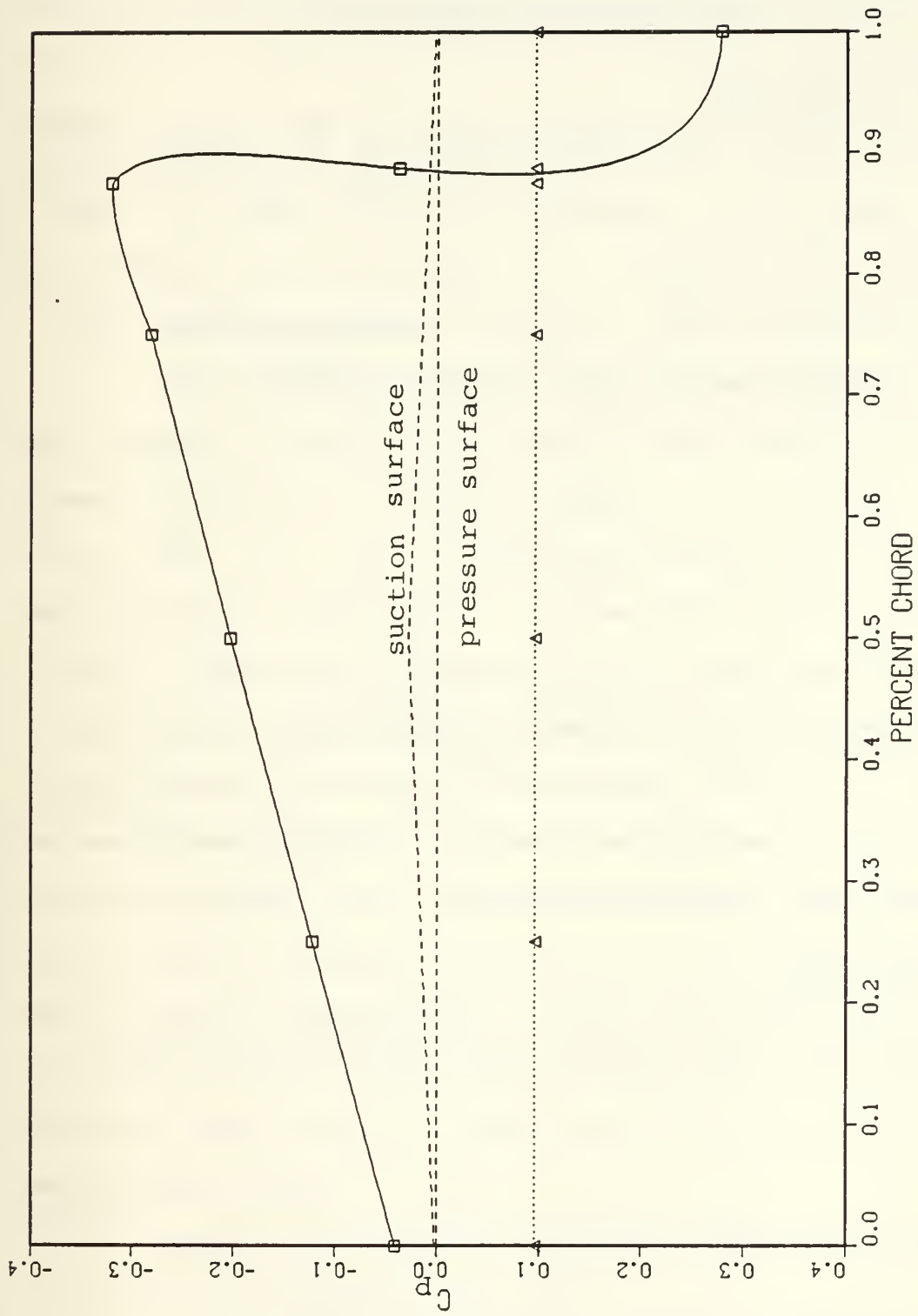


Figure E.2. Blade Pressure Loading Distribution

APPENDIX F
ANALYSIS FROM DESIGN DATA

F1. INLET CONDITIONS

In the design of the cascade model β_1 for minimum loss incidence [Ref. 9] was calculated to be 63° [Ref. 1]. The test section was designed to allow operation with $\beta_1 = 63 \pm 3^\circ$. $\beta_1 = 63^\circ$ was taken to be the design cascade air inlet angle.

The incidence angle [Ref. 9] is defined by

$$i = \beta_1 - \gamma - \frac{\phi}{2} \quad (F-1)$$

γ and ϕ are given in Reference 1. Calculation results in a design incidence angle of 0.91° defined with respect to the mean camber line [Ref. 9]. Adjustment of the test section sidewalls to 3.26° was required to achieve the desired flow incidence (note that the test section sidewalls were referenced to the flat blade pressure surfaces).

F2. TURNING ANGLE

The turning angle through the blade row is given by [Ref. 9]:

$$\Delta\beta = \phi + i - \delta^\circ \quad (F-2)$$

where the deviation angle δ° is given by [Ref. 9]:

$$\delta^\circ = \delta^\circ_0 + m\phi \quad (F-3)$$

The calculation was carried out using a shape correction factor of 0.7, for double circular arc blades, following the design correlations in Chapter 6 in Reference 9. The calculated flow turning angle was 4.3° .

F3. LOSSES

1. Profile Losses

Wake momentum thickness and consequently the loss in total pressure arising from boundary layer growth on the blades is related to velocity diffusion on the blade suction surface [Ref. 9]. The NASA diffusion factor is given by [Ref. 9]:

$$D = \left(1 - \frac{\cos \beta_1}{\cos \beta_2}\right) + \frac{\cos \beta_1}{2\sigma} (\tan \beta_1 - \tan \beta_2) \quad (F-4)$$

for conditions which are planar two-dimensional, with constant through-flow velocity. In Reference 11, experience factors based on supersonic test results were applied to similar design calculations. Linear interpolation between two design points in Reference 11 provided a corrected diffusion coefficient D^* , which was more applicable to compressible flows.

Blade wake momentum thickness parameter (Ω) was computed (following Ref. 24) using:

$$\Omega = 0.005 + 0.16 (D^*)^4 \quad (F-5)$$

The wake momentum thickness parameter is related to the blade profile loss coefficient by

$$\tilde{\omega}_p = \frac{\Omega (2\sigma \cos^2 \beta_1)}{\cos^2 \beta_2} \quad (F-6)$$

2. Secondary Flow

Losses resulting from secondary flow in the passage were computed following Reference 25 using:

$$\tilde{\omega}_i = C_{Di} \left[\frac{\cos^2 \beta_1}{\cos^3 \beta_\infty} \right] \quad (F-7)$$

where

$$C_{Di} = 0.04 C_L^2 \sigma S/h \quad (F-8)$$

and

$$C_L = \frac{2}{\sigma} (\tan \beta_1 - \tan \beta_2) \cos \beta_\infty \quad (F-9)$$

with

$$\tan \beta_\infty = \frac{1}{2} [\tan \beta_1 - \tan \beta_2] \quad (F-10)$$

3. Shock Losses

The shock losses were estimated using the method of Wennerstrom [Ref. 13]. The method assumes the shock to be normal to the inlet relative flow. Upstream Mach number is computed by integrating across the blade passage from the pressure surface to the point of shock impingement on the suction surface. For the present application Mach number at the suction surface was taken from the test data analysis in Appendix E. A five point Simpson's rule numerical integration gave the upstream Mach number. Average total pressure loss through the shock was computed from

$$\tilde{\omega} = \frac{P_{t1} - P_{t2}}{P_{t1} - P_1} \quad (F-11)$$

Table F.1 lists the loss coefficients obtained for the maximum back pressure test condition (for data taken from Appendix E).

F4. BLADE LOADING

Aerodynamic loads on the blades were computed from

$$L/B = C_L q_\infty C \quad (F-12)$$

taken from Reference 1, where

$$q_\infty = \frac{k}{2} P_{t1} M_1^2 \left(1 + \frac{k-1}{2} M_1^2\right)^{-k/k-1} \frac{\cos^2 \beta_1}{\cos^2 \beta_\infty} \quad (F-13)$$

This calculation resulted in a lift force per blade of 7.83 lbf, or only 34.2% of the worst case, steady state load computed in Reference 1.

TABLE F.1
CALCULATED LOSS COEFFICIENTS

<u>Component</u>	<u>Loss Coefficient</u>
Profile	0.025
Secondary Flow	0.001
Shock	0.119
Total	0.145

APPENDIX G

TEST DATA

Results from both first and second phase tests with increasing back pressures are presented here. Run numbers correspond to the Julian date of the test with the suffix indicating specific test number on a given day. Tables G.1 and G.2 contain results obtained with the aluminum blades installed. Results listed in Tables G.3 and G.4 were obtained with the steel blades installed. Pertinent test conditions are listed for each run (note: minimum gap refers to the separation between the drum and ramp of the back pressure control valve).

TABLE G.1
CASCADE TEST 5246-1

Test Conditions:

-2.35° incidence

$P_{to} = 50.0$ PSIA

$P_{ATM} = 14.7$ PSIA

porous wall bleed set at optimum

ramp up, 0% drum

taps 10 & 12 clogged

minimum gap = 0.592 in

<u>Tap No.</u>	<u>Static Pressure</u>	<u>P/P_{to}</u>	<u>M_{is}</u>
1	15.51	0.310	1.40
2	15.67	0.314	1.40
3	15.56	0.311	1.40
4	15.56	0.312	1.40
5	15.74	0.315	1.40
6	15.88	0.318	1.39
7	16.18	0.324	1.38
8	16.25	0.325	1.38
9	16.18	0.324	1.38
10	14.79	0.296	1.44
11	16.24	0.325	1.38
12	14.69	0.294	1.45
13	15.19	0.304	1.42
14	15.33	0.397	1.42
15	14.97	0.299	1.43
16	14.98	0.300	1.43
17	15.46	0.309	1.41
18	15.11	0.302	1.43
19	16.65	0.333	1.36
20	16.12	0.322	1.38

TABLE G.2

CASCADE TEST 5246-2

Test Conditions:

-2.35° incidence

 $P_{to} = 50.0$ PSIA $P_{ATM} = 14.7$ PSIA

porous wall bleed set at optimum

ramp up, 100% drum

tap 10 clogged

minimum gap = 0.592 in

<u>Tap No.</u>	<u>Static Pressure</u>	<u>P/P_{to}</u>	<u>M_{is}</u>
1	15.27	0.305	1.42
2	15.27	0.311	1.40
3	17.51	0.350	1.32
4	17.54	0.351	1.32
5	17.19	0.344	1.34
6	17.28	0.346	1.33
7	17.89	0.358	1.31
8	18.02	0.360	1.30
9	17.91	0.358	1.31
10	14.61	0.292	1.45
11	19.02	0.380	1.26
12	19.12	0.382	1.26
13	17.09	0.342	1.34
14	17.12	0.342	1.34
15	16.91	0.338	1.35
16	16.85	0.337	1.35
17	17.43	0.349	1.32
18	17.15	0.343	1.34
19	16.61	0.332	1.36
20	16.49	0.330	1.36

TABLE G.3

CASCADE TEST 5329-2

Test Condition A:

0.91° incidence

 $P_{to} = 50.0$ PSIA $P_{ATM} = 14.7$ PSIA

porous wall bleed open

ramp up, 0% drum

tap 10 clogged

minimum gap = 0.335 in

<u>Tap No.</u>	<u>Static Pressure</u>	<u>P/P_{to}</u>	<u>M_{is}</u>
1	15.93	0.319	1.39
2	16.94	0.339	1.35
3	17.62	0.352	1.32
4	17.66	0.353	1.32
5	16.86	0.337	1.35
6	16.50	0.330	1.37
7	17.82	0.356	1.31
8	17.87	0.357	1.31
9	17.72	0.354	1.31
10	14.88	0.298	1.44
11	18.96	0.379	1.26
12	18.95	0.379	1.26
13	17.16	0.343	1.34
14	17.40	0.348	1.33
15	16.90	0.338	1.35
16	16.77	0.335	1.35
17	17.50	0.350	1.32
18	17.20	0.344	1.33
19	14.64	0.293	1.45
20	14.96	0.299	1.45

Test Condition B:

0.91° incidence

$P_{to} = 50.0$ PSIA

$P_{ATM} = 14.7$ PSIA

porous wall bleed open

ramp up, 100% drum

tap 10 clogged

minimum gap = 0.335 in

<u>Tap No.</u>	<u>Static Pressure</u>	<u>P/P_{to}</u>	<u>M_{is}</u>
1	15.58	0.312	1.41
2	16.91	0.338	1.35
3	20.35	0.407	1.21
4	20.39	0.408	1.21
5	18.29	0.366	1.29
6	17.76	0.355	1.31
7	20.99	0.420	1.19
8	21.00	0.420	1.19
9	20.98	0.420	1.19
10	14.86	0.297	1.44
11	21.57	0.431	1.17
12	21.65	0.433	1.16
13	19.81	0.396	1.23
14	20.00	0.400	1.22
15	19.51	0.390	1.24
16	19.50	0.390	1.24
17	20.01	0.400	1.22
18	19.79	0.396	1.23
19	14.49	0.290	1.46
20	14.83	0.297	1.44

Test Condition C:

0.91° incidence

$P_{to} = 50.0$ PSIA

$P_{ATM} = 14.7$ PSIA

porous wall bleed set closed (optimum)

ramp up, 100% drum

tap 10 clogged

minimum gap = 0.335 in

<u>Tap No.</u>	<u>Static Pressure</u>	<u>P/P_{to}</u>	<u>M_{is}</u>
1	15.47	0.309	1.41
2	16.38	0.328	1.37
3	23.38	0.468	1.10
4	23.40	0.470	1.10
5	23.19	0.464	1.11
6	22.93	0.459	1.12
7	23.73	0.475	1.09
8	23.77	0.475	1.09
9	23.75	0.475	1.09
10	14.83	0.297	1.44
11	23.64	0.473	1.09
12	23.63	0.473	1.09
13	23.29	0.466	1.10
14	23.30	0.460	1.10
15	22.99	0.460	1.10
16	22.90	0.458	1.12
17	23.28	0.466	1.10
18	22.90	0.458	1.12
19	17.56	0.351	1.32
20	14.47	0.289	1.46

TABLE G.4
CASCADE TEST 5330-2

Test Condition A:

0.91° incidence

$P_{to} = 50.0$ PSIA

$P_{ATM} = 14.7$ PSIA

porous wall bleed set closed (optimum)

ramp down, 0% drum

tap 10 clogged

minimum gap = 0.154 in

<u>Tap No.</u>	<u>Static Pressure</u>	<u>P/P_{to}</u>	<u>M_{is}</u>
1	16.30	0.326	1.37
2	16.20	0.324	1.38
3	12.65	0.253	1.55
4	12.67	0.254	1.55
5	12.94	0.259	1.54
6	12.57	0.251	1.56
7	12.85	0.257	1.54
8	12.83	0.257	1.54
9	12.84	0.257	1.54
10	14.77	0.295	1.44
11	12.71	0.254	1.55
12	12.55	0.251	1.56
13	12.23	0.245	1.57
14	12.24	0.245	1.57
15	12.23	0.245	1.57
16	12.23	0.245	1.57
17	12.51	0.250	1.56
18	12.38	0.248	1.56
19	17.66	0.353	1.32
20	14.54	0.291	1.46

Test Condition B:

0.91° incidence

$P_{to} = 50.0$ PSIA

$P_{ATM} = 14.7$ PSIA

porous wall bleed set closed (optimum)

ramp up, 0% drum

tap 10 clogged

minimum gap = 0.154 in

<u>Tap No.</u>	<u>Static Pressure</u>	<u>P/P_{to}</u>	<u>M_{is}</u>
1	16.21	0.324	1.38
2	16.95	0.339	1.35
3	18.71	0.374	1.27
4	18.75	0.375	1.27
5	17.41	0.348	1.33
6	17.15	0.343	1.34
7	19.45	0.389	1.24
8	19.50	0.390	1.24
9	19.40	0.388	1.25
10	14.71	0.294	1.45
11	19.43	0.389	1.24
12	19.40	0.388	1.25
13	18.39	0.368	1.29
14	18.51	0.370	1.28
15	18.01	0.360	1.30
16	17.98	0.360	1.30
17	18.56	0.371	1.28
18	18.27	0.365	1.29
19	17.78	0.356	1.31
20	14.59	0.292	1.45

Test Condition C:

0.91° incidence

$P_{to} = 50.0$ PSIA

$P_{ATM} = 14.7$ PSIA

porous wall bleed set closed (optimum)

ramp up, 25% drum

tap 10 clogged

minimum gap = 0.154 in

<u>Tap No.</u>	<u>Static Pressure</u>	<u>P/P_{to}</u>	<u>M_{is}</u>
1	16.07	0.321	1.38
2	16.96	0.339	1.35
3	19.35	0.387	1.25
4	19.39	0.388	1.25
5	17.71	0.354	1.31
6	17.35	0.347	1.33
7	19.98	0.400	1.22
8	20.10	0.402	1.22
9	19.97	0.399	1.22
10	14.75	0.295	1.44
11	19.61	0.392	1.24
12	19.61	0.392	1.24
13	18.90	0.378	1.26
14	19.12	0.382	1.26
15	18.58	0.372	1.28
16	18.53	0.371	1.28
17	19.19	0.384	1.25
18	18.74	0.375	1.27
19	17.75	0.355	1.31
20	14.60	0.292	1.45

Test Condition D:

0.91° incidence

$P_{to} = 50.0$ PSIA

$P_{ATM} = 14.7$ PSIA

porous wall bleed set closed (optimum)

ramp up, 50% drum

tap 10 clogged

minimum gap = 0.154 in

<u>Tap No.</u>	<u>Static Pressure</u>	<u>P/P_{to}</u>	<u>M_{is}</u>
1	15.93	0.319	1.39
2	16.96	0.339	1.35
3	21.46	0.429	1.17
4	21.50	0.430	1.17
5	19.52	0.390	1.24
6	19.02	0.380	1.26
7	22.07	0.441	1.15
8	22.11	0.442	1.14
9	22.07	0.441	1.15
10	14.78	0.296	1.44
11	21.90	0.438	1.15
12	21.91	0.438	1.15
13	20.97	0.419	1.19
14	21.10	0.422	1.18
15	20.97	0.419	1.19
16	20.69	0.414	1.20
17	21.14	0.423	1.18
18	20.98	0.420	1.19
19	17.84	0.357	1.31
20	14.60	0.292	1.45

Test Condition E:

0.91° incidence

$P_{to} = 50.0$ PSIA

$P_{ATM} = 14.7$ PSIA

porous wall bleed set closed (optimum)

ramp up, 75% drum

tap 10 clogged

minimum gap = 0.154 in

<u>Tap No.</u>	<u>Static Pressure</u>	<u>P/P_{to}</u>	<u>M_{is}</u>
1	15.62	0.312	1.40
2	16.72	0.334	1.36
3	23.33	0.467	1.10
4	23.34	0.467	1.10
5	23.19	0.464	1.11
6	22.97	0.459	1.12
7	23.78	0.476	1.09
8	23.78	0.476	1.09
9	23.77	0.475	1.09
10	14.73	0.295	1.44
11	23.66	0.473	1.09
12	23.64	0.473	1.09
13	23.18	0.464	1.11
14	23.21	0.464	1.11
15	22.89	0.458	1.12
16	22.85	0.457	1.12
17	23.15	0.463	1.11
18	22.95	0.459	1.12
19	17.64	0.353	1.32
20	14.46	0.289	1.46

Test Condition F:

0.91° incidence

$P_{to} = 50.0$ PSIA

$P_{ATM} = 14.7$ PSIA

porous wall bleed set closed (optimum)

ramp up, 100% drum

tap 10 clogged

minimum gap = 0.154 in

<u>Tap No.</u>	<u>Static Pressure</u>	<u>P/P_{to}</u>	<u>M_{is}</u>
1	15.42	0.308	1.41
2	16.57	0.331	1.36
3	23.72	0.474	1.09
4	23.78	0.476	1.09
5	23.46	0.469	1.10
6	23.19	0.464	1.11
7	24.06	0.481	1.08
8	24.08	0.482	1.08
9	24.05	0.481	1.08
10	14.69	0.294	1.45
11	24.02	0.480	1.08
12	24.01	0.480	1.08
13	23.66	0.473	1.09
14	23.64	0.473	1.09
15	23.30	0.466	1.10
16	23.23	0.465	1.10
17	23.52	0.470	1.10
18	23.35	0.467	1.10
19	17.48	0.350	1.32
20	14.34	0.287	1.46

LIST OF REFERENCES

1. Demo, W.J., Cascade Wind Tunnel for Transonic Compressor Blading Studies, Master's Thesis, Naval Postgraduate School, Monterey, California, June 1978.
2. Volland, K.F., Transonic Cascade Wind Tunnel Modification and Initial Tests, Master's Thesis, Naval Postgraduate School, Monterey, California, June 1980.
3. Starken, H., and Lichtfuss, H., Supersonic Cascade Performance, North Atlantic Treaty Organization Advisory Group for Aerospace Research and Development Report AGARD-LS-39-70, August 1970.
4. Fottner, L., and Lichtfuss, H., "Design of Transonic Compressor Cascades for Minimal Shock Losses and Comparison with Test Results," AGARD-PEP 61 Specialist Meeting on Viscous Effects in Turbomachines, Copenhagen, Denmark, June 1983.
5. Naval Postgraduate School Report NPS67-83-004CR, A Review of the Design of the NPS/TPL Transonic Compressor, by J. Erwin, March 1983.
6. Cornell, D., Experimental Determination of the Relative Flow at the Tip of a Transonic Axial Compressor Rotor, Engineer's Thesis, Naval Postgraduate School, Monterey, California, September 1983.
7. Vasil'ev, L.A., Schlieren Methods, Keter Inc., 1971, pp. 1-18, 95-124, 153-150.
8. Pope, A., and Goin, K.L., High Speed Wind Tunnel Testing, John Wiley & Sons, Inc., 1965.
9. National Aeronautics and Space Administration Special Report, NASA SP-36, Aerodynamic Design of Axial Flow Compressors (NASA SP-36), Edited by I.A. Johnson and R.O. Bullock, 1965.
10. Shapiro, A.H., The Dynamics and Thermodynamics of Compressible Fluid Flow, Vol. I, John Wiley & Sons, New York, 1953.
11. Air Force Propulsion Laboratory, Wright Patterson AFB, Ohio, USAF Project 3066, EDR 7870, Turbine Engine High Flow Compressor Semiannual Technical Report No. 2, by Detroit Diesel Allison, 1973.

12. Prince, D.C., "Rule of Forbidden Signals in a Two-Dimensional Supersonic Compressor Cascade," AIAA Journal, Volume 22, No. 1, January 1984, pp. 157-159.
13. Aero Propulsion Laboratory, Wright Patterson AFB, OH., ASME Paper 83-GT-216, A Three Dimensional Model for the Prediction of Losses in Compressor Blade Rows, by A.J. Wennerstrom and S.L. Puterbaugh, 1983.
14. Naval Postgraduate School Turbopropulsion Laboratory Technical Note, Monterey, California, TPL-TN-86-01, Failure Analysis of 7075-T6 Aluminum Blades for a Transonic Cascade Wind Tunnel, by T. Walsh and T. Salacka, January 1986.
15. Haliday, D., and Resnick, R., Fundamentals of Physics, John Wiley & Sons, New York, 1970, pp. 697-702.
16. Neuhooff, F., Shreeve, R.P., and Fottner, L., Evaluation of the Blade-to-Blade Flow from a High Speed Compressor Rotor, Paper to be presented at the 31 ASME International Gas Turbine Conference & Exhibition, Dusseldorf, W. Germany, June 8-12, 1986 (to be published).
17. Ng, W.F., and Epstein, A.H., Unsteady Losses in Transonic Compressors, ASME Paper 84-GT-183, Massachusetts Institute of Technology, 1984.
18. NASA Lewis Research Center, Cleveland, OH., ASME Paper 84-GT-199, Investigation of Flow Phenomena in a Transonic Fan Rotor Using Laser Anemometry, by A.J. Strazisar.
19. Lawaczeck, O., and Heinemann, H.J., "Von Karman Vortex Streets in the Wakes of Subsonic and Transonic Cascades," AGARD-PEP--Meeting on Unsteady Phenomena in Turbomachinery, Monterey, California, AGARD Conf. Proceedings, No. 177, September 1975.
20. Heinemann, H.J., Lawaczeck, O., and Butefisch, K.A., "VonKarman Vortices and their Frequency Determination in the Wakes of Profiles in the Sub- and Transonic Regimes," IUTAM Symposium Transonicum II, Edited by K. Oswatitsch and D. Rues, Springer Verlag, New York, 1976.
21. Heinemann, H.J., and Butefisch, K.A., "Determination of the Vortex Shedding Frequency of Cascades with Different Trailing Edge Thicknesses," AGARD-PEP--Meeting on Unsteady Phenomena in Turbomachines, AGARD Conf. Proceedings, No. 227.
22. Zucker, R.D., Fundamentals of Gas Dynamics, Matrix Inc., Beaverton, Oregon, 1977, pp. 83-105.

23. Inger, G.R., Transonic Shock/Turbulent Boundary-Layer Interaction on Curved Surfaces, AIAA Paper 81-1244, University of Colorado, 1981.
24. Kerrebrock, J.L., Flow in Transonic Compressors, AIAA Paper 80-0124, Massachusetts Institute of Technology, 1980.
25. Vavra, M.H., Aero-Thermodynamics and Flow in Turbomachines, John Wiley & Sons, New York, 1960, pp. 375-393.

INITIAL DISTRIBUTION LIST

	No. Copies
1. Defense Technical Information Center Cameron Station Alexandria, Virginia 22304-6145	2
2. Library, Code 0142 Naval Postgraduate School Monterey, California 93943-5002	2
3. Department Chairman, Code 67 Department of Aeronautics Naval Postgraduate School Monterey, California 93943-5000	1
4. Director Turbopropulsion Laboratory Code 67Sf Naval Postgraduate School Monterey, California 93943-5000	8
5. LCDR Michael G. Hegland, USN USS Tripoli (LPH-10) FPO, San Francisco, Calif. 96626-1645	2
6. Mr. George Derderian Naval Air System Command Code AIR-310E Department of the Navy Washington, D.C. 20360	1
7. Commander Naval Air Propulsion Center (Attn: V. Lubosky) P.O. Box 7176 Trenton, New Jersey 08628	1

217456

Thesis
H4223
c.1

Hegland

Investigation of a
mach 1.4 compressor
cascade with variable
back pressure flow
visualization.

217456

Thesis
H4223
c.1

Hegland

Investigation of a
mach 1.4 compressor
cascade with variable
back pressure flow
visualization.



thesH4223

Investigation of a mach 1.4 compressor c



3 2768 000 65866 0

DUDLEY KNOX LIBRARY